FABRICATION OF GRADED-INDEX PLASTIC OPTICAL FIBER BY THE DIFFUSION-ASSISTED COEXTRUSION METHOD

By

IN-SUNG SOHN

A DISSERTATION PRESENTED TO THE GRADUATE SCHOOL
OF THE UNIVERSITY OF FLORIDA IN PARTIAL FULFILLMENT
OF THE REQUIREMENTS FOR THE DEGREE OF
DOCTOR OF PHILOSOPHY

UNIVERSITY OF FLORIDA

2001

To my wife, Hyun-Su Lee, and my daughter, Ye-Bin

ACKNOWLEDGMENTS

I would first like to acknowledge my supervisory committee. To Dr. Chang-Won Park, my advisor, I would like to give thanks and appreciation for his support and guidance throughout my doctoral research. I would like to extend my gratitude to my other committee members, Dr. Spyros Svoronos, Dr. Richard B. Dickinson and Dr. Anthony B. Brennan for all their interest in my work and helpful comments and suggestions.

I would also like to express my gratitude to Mr. Juan C. Cutie of Cyro Industries for providing PMMA samples, and special thanks are due to Mr. Gary Scheiffele of the Engineering Research Center at the University of Florida and Dr. Jung-Sik Hwang at the McMaster University for their assistance in FT-IR and UV-vis measurements.

In addition, I gratefully acknowledge the partial support provided by Nanoptics, Inc., and I would like to thank Saehan Industries Inc. for allowing me to study in the University of Florida. I would also like to give thanks to all the colleagues and friends in the chemical engineering department for their encouragement, advice and the great times we have had together.

I am extremely grateful to my parents and parents-in-law. Without their unending love and support, this work would not have been possible. Finally, but not least, I would like to thank my wife, Hyun-Su Lee, and my daughter, Ye-Bin, whose patience, sacrifice and love enabled me to complete this work, and made my life fruitful.

TABLE OF CONTENTS

Page

ACKNOWLEDGEMENTS iii

ABSTRACT vi

CHAPTERS

1 GENERAL INTRODUCTION 1

1-1 Plastic Optical Fiber 1
1-2 Principles of Fiber Optics 2
  1-2-1 Classification of Optical fibers 3
  1-2-2 Total Internal Reflection 4
  1-2-3 Classification of Rays 6
  1-2-4 Acceptance Angle and Numerical Aperture 9
1-3 Electromagnetic Theory for Optical Waveguides 11
  1-3-1 Electromagnetic Waves 11
  1-3-2 Phase Shifts and Guided Modes in a Waveguide 13
  1-3-3 Dispersion 14
1-4 Advantages of GRIN Fibers 15
  1-4-1 Channel Capacity 15
  1-4-2 Attenuation 19

2 MODELING OF GI POF FABRICATION PROCESS 23

2-1 Introduction 23
2-2 Diffusion-Assisted Coextrusion Process 24
  2-2-1 Modeling 26
  2-2-2 Simulation Results and Discussion 29
  2-2-3 Multi-layer Fibers 35
2-3 Estimation of Bandwidth 37
  2-3-1 Ray Optical Formulation of Impulse Response Function 37
  2-3-2 Impulse Response Curves and Bandwidths 41
  2-3-3 WKB Approximation 45
2-4 Summary 46

3 FABRICATION AND CHARACTERIZATION OF GRIN POF 48

- 3-1 Preparation of GRIN Fibers 48
  - 3-1-1 DPS-Doped GRIN Fibers 49
  - 3-1-2 Oil Red EGN-Doped GRIN Fibers 54
- 3-2 Temperature Dependence of Diffusivity 58
- 3-3 Stability of Refractive Index Profiles 63
- 3-4 Estimation of Bandwidth 66
- 3-5 Summary 70

4 ANNULUS DIFFUSION SYSTEM 72

- 4-1 Introduction 72
- 4-2 Modeling 72
- 4-3 Reliability of the Approximate Solutions 77
- 4-4 Non-Newtonian Effect 79
- 4-5 Experimental 80
- 4-6 Results and Discussion 82
- 4-7 Estimation of Bandwidth 86
- 4-8 Summary 89

5 CONCLUSIONS 91

APPENDICES 94

A DERIVATION OF SERIES SOLUTION IN CYLINDRICAL COORDINATE SYSTEM 94

B DERIVATION OF SERIES SOLUTION IN CARTESIAN COORDINATE SYSTEM 98

REFERENCES 101

BIOGRAPHICAL SKETCH 106

Abstract of Dissertation Presented to the Graduate School
of the University of Florida in Partial Fulfillment of the
Requirements for the Degree of Doctor of Philosophy

FABRICATION OF GRADED-INDEX PLASTIC OPTICAL FIBER BY THE DIFFUSION-ASSISTED COEXTRUSION METHOD

By

In-Sung Sohn

December 2001

Chairperson: Chang-Won Park
Major Department: Chemical Engineering

Recently, plastic optical fibers (POFs) have drawn significant attention as high-speed transmission media due to their advantages over conventional glass optical fibers such as flexibility and durability. In addition, Grade-Index (GRIN) POFs with smoothly varying refractive indices provide increased data transmission speeds suitable for the short-distance communications such as local area networking or home networking.

In this research, the *diffusion-assisted coextrusion process* is introduced as a method to fabricate GRIN POFs. In this process, two or more polymeric materials containing additives for refractive index modification are fed separately into a coextrusion die where a concentric multi-layer structure is formed. Subsequently, the diffusion of additives take places in a diffusion zone creating a non-equilibrium concentration profile, hence the refractive index profile.

A theoretical analysis for the prediction of the refractive index profile obtainable by this process indicates that it is difficult to obtain a near-parabolic refractive index profile with the tubular flow design unless a very large residence time in the diffusion zone is provided. However, significant changes in the refractive index profile can be induced by adopting a multi-layer approach and an annulus flow design. Furthermore, the bandwidth estimated by the ray analysis indicates that even a small variation of the refractive index profile created by the additive diffusion can result in a significant increase in the bandwidth.

To verify the findings from theoretical analysis, poly(methyl methacrylate)-base GRIN POFs with diphenyl sulfide and diphenyl sulfoxide as refractive index-modifying dopants were prepared and the effects of various operating conditions such as melt temperatures, flow rates and core-cladding interface positions were investigated. The dopant concentration profile, thus the refractive index profile, characterized by FT-IR spectroscopy, has been shown to be controllable by adjusting the material and/or process variables.

Through the theoretical analysis and experimental verifications, it was shown that bandwidth over 700 MHz at a 100 m distance could be obtained by this method, suggesting that the diffusion-assisted coextrusion process is a viable method to fabricate a high bandwidth GRIN POF that is applicable for short-distance communications.

CHAPTER 1
GENERAL INTRODUCTION

1-1 Plastic Optical Fiber

Recently, plastic optical fibers (POFs) have drawn significant attention as high-bandwidth data-transmission media for local area networks or home networks. In spite of their higher attenuation than glass optical fibers (GOFs), POFs are perceived to be more suitable for these applications due to their flexibility and durability. These properties make it possible for POFs to have much larger core diameters in the order of 1 mm compared to 5–10 μm of single-mode GOFs.[1] Since large diameter makes splicing of optical fibers much easier and allows us to use lower cost light sources and connectors, the economic advantage is very significant.

It was in the late sixties when the first POF was commercially developed by Du Pont, for display purposes.[2] Since then, developments in POF fabrication have focused mainly on lowering transmission losses caused by various sources of intrinsic and extrinsic origins. In the early seventies, Mitsubishi Rayon patented their continuous spinning process for high purity acrylics, and this resulted in the development of ESKA™ POF, with minimum losses in the region of 120 dB/Km at 567 nm.[2]

The theoretical minimum attenuation of PMMA core POF is about 100 dB/Km at the wavelength of 650 nm, which restricts their application to distances of 100 m at most. A recent study, however, found that about 90% of all desktop applications are located within 80 m from a node center,[3] opening a bright future for POF in the applications of short-distance communications. The transmission loss limit of POF has been further lowered to 6 dB/km by adopting fluorinated and/or deuterated PMMA as core material.[4]

With the progress in the development of low-loss fibers and advances in optical source technology, applications of POF have been expanded from simple light displays to optical sensors, short-distance data communication such as local area networking (LAN), and data links in automobiles and aircraft. In addition, POFs can have higher numerical apertures than GOFs, trapping more lights. Therefore, using POFs is also advantageous in image guide applications such as endoscopes and industrial fiberscopes.

While standard POFs, whose refractive index difference between core and cladding is in a step index profile, have limited bandwidths (lower than about 10 MHz·Km), graded index (GI or GRIN) POFs provide increased signal bandwidths due to their smoothly varying refractive indices. Thus, GRIN POFs are expected to be used more extensively as high-speed optical signal transmission media in the near future.

The materials for POFs are preferably amorphous homopolymers than copolymers to minimize transmission losses. Fibers with poly(methyl methacrylate) (PMMA) cores are currently dominant in commercial applications. Other polymers such as polycarbonate (PC) and polysiloxane are also used for POFs for their higher heat resistance.[4]

1-2 Principles of Fiber Optics

Propagation of light in an optical fiber is described by Maxwell's equations since light itself is an electromagnetic wave. However, it is well known that classical geometric optics provides an approximate description of light propagation when the refractive index varies only slightly over a distance comparable to the wavelength of light. In geometric optics, light is considered to propagate in a straight line in a homogeneous medium in the direction normal to the equi-phase plane of electromagnetic wave. It has been shown that optical waveguides must be multimoded with $2\pi R n_1 \theta_c / \lambda \gg 1$ for geometric optics to be valid.[5] Here R is the radius of core, n_1 is the maximum refractive index of core material, θ_c is the critical angle and λ is the free-space wavelength of the light. In this research, geometric optics is adopted for the estimation of bandwidth characteristics of optical fibers for its simplicity although several electromagnetic concepts are introduced for more through understanding of the underlying principles of fiber optics.

1-2-1 Classification of Optical fibers

Optical fibers are classified into two main categories. One is the *step index* (SI) fiber and the other the *graded index* (GI or GRIN) fiber. The SI fibers consist of the core with higher refractive index materials and cladding with lower refractive index materials. The refractive index profile for this type of fiber makes a step change at the core-cladding interface as indicated in Figure 1-1a. On the other hand, GRIN fibers do not have a constant index in the core, but a smoothly varying index profile over the fiber radius with a maximum value of n_1 at the axis and a constant value n_2 beyond the core radius R in the cladding (Figure 1-1b).

Graded-index fibers exhibit far less intermodal dispersion than step index fibers due to their refractive index profile. Although many different modes are excited in the GRIN fiber, the different group velocities of the modes tend to be normalized by the index grading. In geometric optical perspective, the rays traveling close to the fiber axis have shorter paths compared with rays that travel in the outer region of the core. However, the near axial rays are transmitted through a region of higher refractive index, and hence they

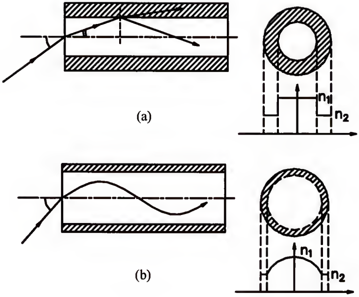

Figure 1-1 Schematic of optical fibers
(a) Step index fiber (b) Graded index fiber

travel with lower velocities. This compensates the shorter path lengths and reduces dispersion in the fiber.

1-2-2 Total Internal Reflection

One of the most important phenomena in optical waveguide theory is the *total internal reflection.* Figure 1-2 illustrates waves incident at an angle, θ_1 on a dielectric interface from the high refractive index side.

In the Figure 1-2a, the refracted ray in the low index medium exits at an angle θ_2, and according to Snell's law, the exit angle is given by

$$\theta_2 = \sin^{-1}\left(\frac{n_1}{n_2}\sin\theta_1\right) \qquad (1\text{-}1)$$

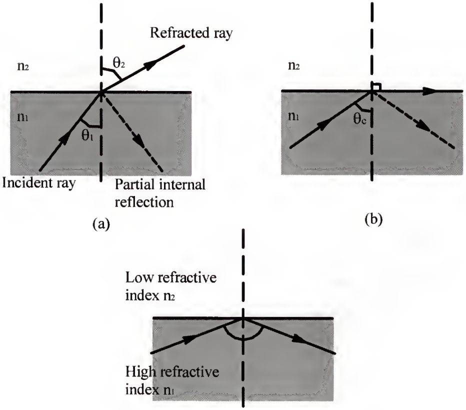

(a) (b)

(c)

Figure 1-2 Three cases in which the angle of incidence is (a) below (b) at (c) above the critical angle.

As the angle of incidence θ_1 increases, the angle of refraction θ_2 must also increase, and the refraction angle reaches a value of 90° when

$$\sin\theta_1 = \frac{n_2}{n_1} \tag{1-2}$$

This value of θ_1 is known as the *critical angle* θ_c. At the critical angle θ_c, the refracted ray travels along the interface (Figure 1-2b), and for an angle larger than the critical angle θ_c, the ray will be totally reflected at the interface (Figure 1-2c). Consequently, the light will be trapped and guided through successive total internal reflections within the high refractive index medium when the high refractive index medium is enclosed by the low refractive index medium.

1-2-3 Classification of Rays

In geometric optics, the trajectory of a light ray in a dielectric medium is described by the following Eikonal equation:[6]

$$\frac{d}{ds}\left(n\frac{d\mathbf{r}}{ds}\right) = \nabla n \tag{1-3}$$

where **r** is the position vector of a point on the ray path and *s* is the arc length of the propagating ray measured from a fixed point along the trajectory. In Figure 1-3, ray paths in an SI optical fiber with core radius *R* are depicted.

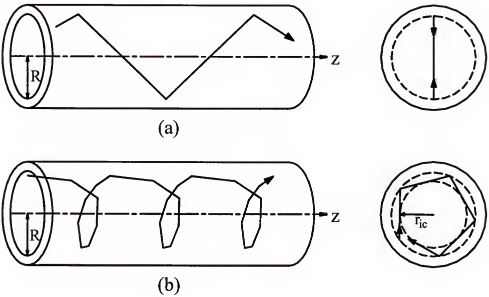

Figure 1-3 Ray paths in an SI fiber
(a) meridional ray (b) screw ray

It is often convenient to distinguish between rays whose travel paths sit on the plane possessing the fiber axis (Figure 1-3a) –known as *meridional rays* – and rays that never pass through the fiber axis–known as *screw rays* (Figure 1-3b). Meridional rays lie in a plane with the width of $2R$, whereas screw rays follow a helical path, whose projection onto the cross section of the fiber is polygonal–although not necessarily closed. While meridional rays are bound by a cylinder with radius R, the screw rays are bound by two cylindrical surfaces. The radius of the inner surface is r_{ic}, known as the inner caustic, and the outer radius is the core radius R for an SI fiber and the turning point caustic r_{tp} for a GRIN fiber. The trajectory of a screw ray path in a GRIN fiber is sinusoidal compared to the zigzag pattern of a meridional ray as illustrated in Figure 1-4.

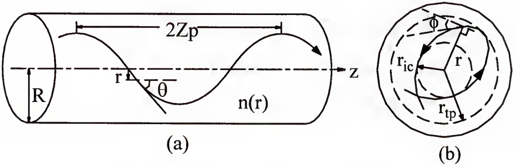

(a)

(b)

Figure 1-4 A screw ray path in a GRIN fiber

The direction of a propagating ray at a radial position r can be defined by two angles θ and ϕ. Here θ is the angle between the tangent line to the ray and the fiber axis (i.e., z-axis), and ϕ is the angle that the projection of the tangent line onto the fiber cross section makes with the azimuthal direction (Figure 1-4). In the previous section, θ meant the incident angle a ray makes with the normal to the interface of two materials.

However, it will be used to describe the angle with the fiber axis hereafter. It can be shown from equation 1-3 that two parameters κ and *l* defined by the following two equations remain constant along a given ray path. Thus, all rays propagating in a fiber can be completely defined by these two invariants.[5]

$$\kappa = n(r)\cos\theta \tag{1-4}$$

$$l = \frac{r}{R} n(r)\sin\theta\cos\phi \tag{1-5}$$

Here κ accounts for the translational invariance of the fiber along its axis, whereas *l* is related to the skewness of a ray. Both θ and ϕ are also functions of position *r*.

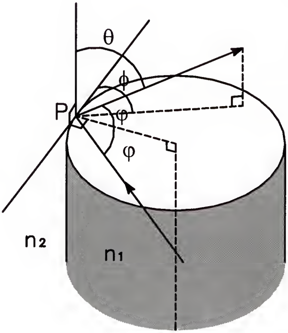

Figure 1-5 Angles for describing reflection of a ray incident at P on the interface of a step-index fiber. The angle of incidence is φ. The incident and reflected rays make angles θ with axial direction.

From the Snell's law, we know that a ray will refract at point P in Figure 1-5 if $\varphi < \varphi_c$, where φ_c is the critical angle defined by

$$\sin\varphi_c = n_2/n_1 = \cos\theta_c \tag{1-6}$$

and will undergo total internal reflection if $\varphi > \varphi_c$. However, not all rays with $\varphi > \varphi_c$ are bound, but only certain rays among these rays satisfying this condition are bound. It can be derived from the equation 1-3 that the condition for a ray to be bound in a fiber is $0 \le \theta \le \theta_c$, independent of ϕ.[5] The remaining rays that are not included in either bound or refracting rays belong to a third class of rays called tunneling rays. The name tunneling is derived from the fact that these rays appear to tunnel a finite distance into the cladding, and lose power to the cladding. Electromagnetic wave in this region is evanescent and decays exponentially with radial position. Rays that are not bound, that is, tunneling and refracting rays, are called leaky rays.

It can be shown that all the rays satisfying the following inequality are trapped and guided by the optical fiber,

$$n_2 \le \kappa \le n_1 \tag{1-7}$$

As was mentioned previously, n_1 and n_2 are the refractive indices at the center and at the outer edge of the optical fiber.

1-2-4 Acceptance Angle and Numerical Aperture

Since only rays with a sufficiently large incident angle (φ in Figure 1-6) at the core-cladding interface are transmitted by total internal reflection, it is clear that not all rays entering the fiber will continue to propagate to the end of the fiber. Meridional rays that are incident at any point on the circular disc of the core will be guided only if their corresponding angle of refraction is less than θ_c, that is, if the angle of incident θ_0 in the exterior medium of refractive index n_o is less than a certain limiting angle of acceptance θ_{ACC}. This situation is illustrated in Figure 1-6.

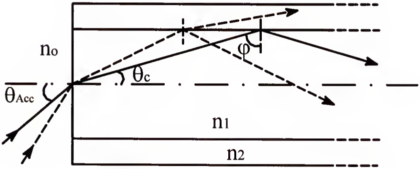

Fig.1-6 The ray paths for meridional rays launched into an SI fiber in air

In addition, the acceptance angle is related with the refractive indices of the media involved. When the refractive indices of core, cladding and surrounding media are n_1, n_2, n_0, Snell's law gives the following relation (Figure1-6):

$$n_0 \sin\theta_{ACC} = n_1 \sin\theta_c \qquad (1\text{-}8)$$

Here the quantity $n_1\sin\theta_c$ is the *numerical aperture* (NA). If the angle between the fiber axis and the light ray entering the fiber is smaller than the acceptance angle, the light ray is guided through the core of the fiber by total internal reflections. Thus, the bigger the NA, the greater the amount of light that passes through the fiber, making the transmitted power greater. In case of step-index GOFs, both core and cladding materials are silica glass with slightly different material compositions. Consequently, their numerical apertures are typically as small as about 0.1 resulting in acceptance angles of about 6°. Plastic optical fibers, on the other hand, have a broader choice of core and cladding materials. Thus, the NA of a SI POF can be as high as 0.5, which results in an acceptance angle of 30°.[7]

It can be easily shown that the numerical aperture for SI fibers is equal to

$$NA_{SI} = \sqrt{\left(n_1^2 - n_2^2\right)} \tag{1-9}$$

The numerical aperture of a GRIN fiber, however, is defined differently from SI fiber because the refractive index varies continuously across the fiber radius. The effective numerical aperture of the input cross section for a GRIN fiber is given by[8]

$$NA_{GI} = \frac{1}{\sqrt{2}}\sqrt{\left(n_1^2 - n_2^2\right)} \tag{1-10}$$

1-3 Electromagnetic Theory for Optical Waveguides

Although ray optics were adopted in this research for its simplicity, electromagnetic wave theory must be considered for an improved model and a better understanding of the propagation of light in optical fibers. In this section, basic principles underlying wave propagation and modal dispersion are introduced.

1-3-1 Electromagnetic Waves

When light is described as an electromagnetic wave, it consists of a periodically varying electric field **E** and magnetic field **H**, which are oriented at right angles to each other and to the propagation direction of light.

Starting from the source-free Maxwell's equations, two wave equations can be derived to describe the propagation of light in a medium having electric permitivity ε and magnetic permeability μ:[5]

$$\nabla^2 \mathbf{E} = \mu\varepsilon \frac{\partial^2 \mathbf{E}}{\partial t^2}$$
$$\nabla^2 \mathbf{H} = \mu\varepsilon \frac{\partial^2 \mathbf{H}}{\partial t^2} \qquad (1\text{-}11)$$

Here, **E** and **H** represent electric and magnetic field vectors, ∇^2 is the vector Laplacian operator, and the refractive index n is related with the permeability and permitivity by

$$n = \sqrt{\frac{\varepsilon\mu}{\varepsilon_0 \mu_0}} \qquad (1\text{-}12)$$

where ε_0 and μ_0 are electric permitivity and magnetic permeability in vacuum, respectively.

The above equations hold for every component of **E** and **H** field, and can be solved independently once a proper coordinate system is chosen in such a way that there is no coupling between orthogonal components.[9]

The electric and magnetic field vectors **E**(x, y, z) and **H**(x, y, z) are each separated into two parts. One part represents the power that is guided without attenuation along the waveguide, and the remaining part represents the power that is radiated from the waveguide. The guided or bound portion is expressed as a finite sum of bound modes:[5]

$$\mathbf{E}(x,y,z) = \sum_i a_i \mathbf{E}_i(x,y,z) + \mathbf{E}_{rad}(x,y,z)$$
$$\mathbf{H}(x,y,z) = \sum_i a_i \mathbf{H}_i(x,y,z) + \mathbf{H}_{rad}(x,y,z) \qquad (1\text{-}13)$$

An optical mode refers to a specific solution of the wave equation that satisfies appropriate boundary conditions and has the property that its spatial distribution does not change with propagation. Electromagnetic modes can be regarded as transverse resonances of the fields of the waveguide, which may be analogous to the normal modes of vibration of a membrane fixed at its periphery. While the membrane has an infinite number of bound modes, an optical waveguide can only support a finite number of bound modes.[9]

1-3-2 Phase Shifts and Guided Modes in a Waveguide

The physical structure of electromagnetic modes can be better understood by considering interference of plane waves traveling in opposite directions. This situation is illustrated in Figure 1-7 for a planar waveguide with a step index profile. Being excited by the same source, the waves are coherent with one another at a given plane in the waveguides, so they form stable interference patterns. When the two waves interfere constructively, the electric field is a maximum, and where destructive interference occurs, the intensity is minimum. In Figure 1-7, TE_0 (Transverse Electric: the electric field is

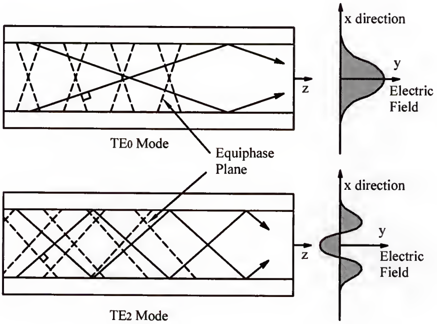

Figure 1-7 Interference of two plane waves at slightly different angles in a planar waveguide form modes

normal to the plane of incidence) and TE_2 modes are depicted. The subscripts 0 and 2 are called modal numbers, and are assigned to each mode starting from zero. Every mode has stable field distribution in the x direction with only periodic z dependence.

On planar waveguides, TE and TM (Transverse Magnetic: the magnetic field is normal to the plane of incidence) modes correspond to the two possible polarization states of the electromagnetic field. In either case, the direction of electric or magnetic field is not altered after reflection, so that either z component of **E** or **H** is conserved, and TE and TM modes do not mix.

On circular fibers, on the other hand, only meridional rays can preserve z components of **E** or **H** at every reflection. Thus only meridional rays can make up TE and TM modes on round waveguides. For screw rays, it is not possible to maintain TE and TM polarization as we follow the direction of light since the radial and azimuthal components are tightly coupled in the wave equation. Instead, two types of hybrid modes (EH and HE modes depending upon the relative magnitude of longitudinal E and H components), having both longitudinal H and E components in the waveguide correspond to screw rays.

1-3-3 Dispersion

Dispersion refers to the spreading of a signal in time, which limits the information-carrying capacity of a communication channel. The dispersion in optical waveguides is caused by two mechanisms.

First, the pulse energy in a waveguide will be distributed among the various allowed modes, and different modes have different group velocities. Thus, it spreads out as it propagates. This type of pulse spreading is called *intermodal dispersion*, or simply modal dispersion, and is the dominant cause of pulse spreading in multimode fibers. There are several ways to counter modal dispersion. The obvious solution is to use a waveguide that supports only one mode; hence a single-mode waveguide. Most high-speed, long-distance optical fibers used throughout the world today are single mode fibers. The second solution is to use graded-index fibers. A graded index reduces the geometric path difference between lower-order and higher-order modes.

The second cause of pulse spreading, *material dispersion*, is related with the small, yet finite bandwidth of the light source. Since different wavelengths of light travel at different velocities within the medium, the input pulse will effectively spread in time. The total pulse broadening due to both modal and material dispersion is simply the quadratic sum of each contribution:[9]

$$\tau_{tot} = \left(\tau_{modal}^2 + \tau_{mat}^2\right)^{1/2} \tag{1-14}$$

since they affect pulse broadening independently, and the combined effect of two independent Gaussian events is the convolution of them.

1-4 Advantages of GRIN Fibers

1-4-1 Channel Capacity

Due to the dispersion of an input pulse discussed in the previous section, there exists maximum bit rate obtainable for an optical channel.

An estimate of the maximum bit rate of an optical channel with dispersion may be obtained by considering the light pulses at the output to have a Gaussian shape with an rms width of σ in seconds. The maximum bit rate B_T is given approximately by [8]

$$B_T(\max) \approx \frac{0.25}{\sigma}\ \text{bit/s} \tag{1-15}$$

The conversion of bit rate to bandwidth in Hertz depends on the digital coding format used. When a non-return to zero code is employed, the binary one level is held for the whole bit period. There are two bit periods in one wavelength in this case (i.e., two bits per second per hertz), as illustrated in Figure 1-8a. Hence, the maximum bandwidth B is one half of the maximum data rate:

$$B_T(\max) = 2BW \tag{1-16}$$

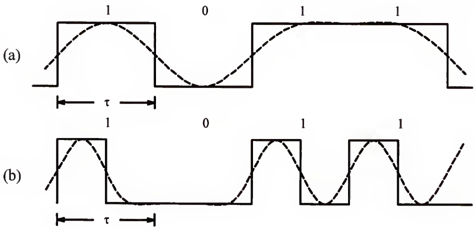

Figure 1-8 Relationship between bit rate and bandwidth
(a) Non-return to zero code (NRZ) (b) Return to zero code (RZ)

However, when a return to zero code is adopted, the data rate is equal to the bandwidth in hertz (i.e., one bit per second per hertz). When the limitations in the bandwidth of a fiber due to dispersion are considered, it is normally with regard to a return to zero code.[1]

Another widely used measure of bandwidth is FWHM (full width at half maximum), which is more appropriate when the shape of the output signal is far from Gaussian. This measures the width of a response curve at half of the maximum height as illustrated in Figure 1-9, and the bandwidth B is given by 0.45/FWHM.[8]

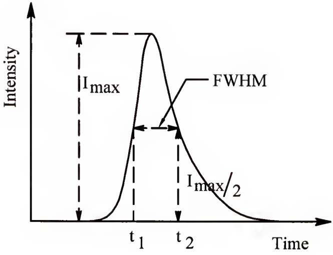

Figure 1-9 Illustration of Full width at half maximum bandwidth

The pulse broadening of an optical signal in optical fibers increases linearly with fiber length, and thus the bandwidth is inversely proportional to distance. Therefore, bandwidth-length product (i.e., $B \times L$ MHz·Km) is often adopted as a more useful parameter for the information-carrying performance of a transmission medium.

The bandwidth of a GRIN fiber is well known to be strongly affected by the refractive index profile of the fiber.[10-12] Figure 1-10 shows the dependence of the bandwidth on the refractive index profile when the refractive index of a GRIN fiber is given by a power law profile as in equation 1-17:

$$n(r) = n_1 \left[1 - 2\Delta \left(\frac{r}{R} \right)^{\alpha} \right]^{1/2} \tag{1-17}$$

In Figure 1-11, several refractive index profiles of power-law fiber are plotted. As α increases, the index profile becomes flatter at the fiber center, and $\alpha = \infty$ represents an SI fiber. In the particular case where $\alpha = 2$, the power law is called a "parabolic law." This

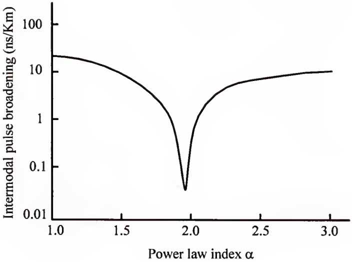

Figure 1-10 The intermodal pulse broadening for GRIN fibers having Δ = 0.01 for various power law index

parabolic profile has special importance because the maximum bandwidth for a GRIN fiber is attainable near $\alpha = 2$ as shown in Figure 1-10.

Although it is not possible to contrive a profile that completely eliminates modal dispersion except for the hyperbolic secant profile in planar waveguide, it is known that the bandwidth of an optical fiber is maximized when[7]

$$\alpha = 2 - \frac{12}{5}\Delta \qquad (1\text{-}18)$$

Here, Δ is defined as

$$\Delta = \frac{n_1^{\,2} - n_2^{\,2}}{2n_1^{\,2}} \qquad (1\text{-}19)$$

and 2Δ is approximately the relative index difference when the index difference is small, which is the typical case in optical transmission.

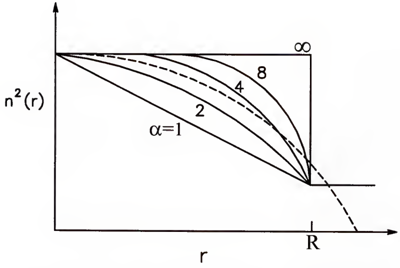

Figure 1-11 Power law index profiles for various α values.
Dashed line: hyperbolic secant profile

1-4-2 Attenuation

The transmission loss of the light, also known as attenuation, is measured in decibel (dB) per kilometer using equation 1-20 from input power I and output power I_0 and the fiber length L in kilometer:

$$\Phi(\mathrm{dB/Km}) = \frac{10}{L}\log\left(\frac{I}{I_0}\right) \tag{1-20}$$

About 3 dB corresponds to an intensity loss of about 50%. Thus, if an optical fiber has an attenuation of 3 dB/km, the light signal will retain about 50% of its intensity when it travels a distance of 1 km through the fiber. Very high quality GOFs made for communications can have attenuation as low as 0.5 dB/km, whereas typical POFs have attenuation of about 150 dB/km. For this reason, POFs cannot be used for long distance communications.

Table 1-1. Loss mechanisms of POF[4]

Intrinsic		Extrinsic	
Absorption	Scattering	Absorption	Scattering
Higher harmonics of CH absorption	Raleigh scattering ($\propto 1/\lambda^4$)	Transition metals	Dust and microvoids
Electronic transition		Organic contaminants	Fluctuation of core diameter
			Orientational birefringence
			Core-cladding boundary imperfection

The loss mechanisms of POF and their magnitudes for PMMA core SI fibers are listed in Table 1-1. Intrinsic absorption losses include higher harmonics of molecular vibration in the IR region and electronic transitional absorption in the UV region. Scattering losses include so-called Rayleigh scattering and loss due to imperfections in the waveguide structure. Among the loss factors listed above, the most significant ones are vibrational absorption due to carbon-hydrogen bonds and Rayleigh scattering caused by structural irregularities within the core of optical fibers, since the losses attributable to extrinsic factors can be reduced by appropriate fiber fabrication processes. Eliminating CH vibrational absorption losses can be achieved by deuteration and fluorination of PMMA, and the theoretical loss limit of PMMA-base POF was reported as 5.8 dB/Km at 650 nm.[13]

In Figure 1-12, the loss spectrum of PMMA core POF is shown. Although the ultimate loss limit is 35 dB/Km at 568 nm, the preferred transmission window is 650 nm

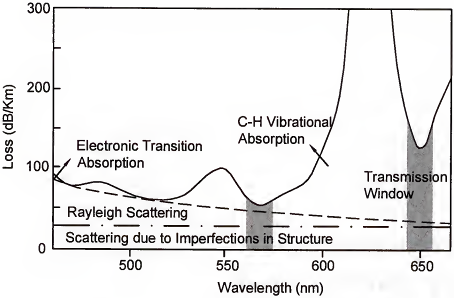

Figure 1-12 Transmission loss and loss factors of PMMA core POF[4]

where GaAlAs LEDs are available. Compared to the GaP LED whose wavelength is in the green region, GaAlAs LED, emitting red light, has higher emission power.[14] As shown in Table1-2, a part of extrinsic scattering loss of an SI fiber is caused by the structural irregularity of the core-cladding interface, which does not exist in the GRIN fibers since the light rays pass through the fiber with sinusoidal trajectories without touching the wall.[15]

Table 1-2. Loss factors and limits of PMMA core POF[1]

Loss Factor	Wavelength (nm)		
	516	568	650
Total Loss	57	55	126
Absorption	11	17	96
Rayleigh Scattering	26	18	10
Structural Imperfections	20	20	20
Loss Limit	37	35	106

CHAPTER 2
MODELING OF GRIN POF FABRICATION PROCESS

2-1 Introduction

There are only several methods known for the fabrication of GRIN-POFs. The best known may be the *interfacial-gel polymerization method*, which was pioneered by Koike.[7, 10-12, 15-21] In this method, a polymeric tube [e.g., poly(methyl methacrylate) (PMMA) tube] is filled with a monomer (e.g., methyl methacrylate) containing a non-reacting dopant, which raises the refractive index of PMMA when dispersed in the polymer matrix. The inner wall of the tube is swollen by the monomer forming a gel phase. When polymerization reaction is induced by heat or other means, polymerization takes place in the gel phase more preferentially, and the thickness of the plastic tube grows inward eventually forming a rod. Since the non-reacting dopant added to the monomer is rejected from the reacting site due to either lower diffusivity or solubility as the reaction progresses, the dopant concentration becomes gradually higher toward the center of the rod. Consequently, a refractive index profile is created in the radial direction of the rod. The resulting rod (or preform) is then drawn to a fiber by the thermal drawing method. It has been reported that GRIN-POF with a bandwidth of 2 GHz for 100 m (gigabits per second for 100m) could be fabricated successfully by this technique.

Van Duijnhoven and Bastiaansen[22] reported another fabrication method for GRIN-POF that utilizes centrifugal force during polymerization reaction. In their method, a polymer such as poly(methyl methacrylate) or poly(tetrafluoropropyl methacrylate) is dissolved in a monomer which has higher refractive index and lower density in a tubular reactor. By heating and rotating the reactor at a high speed, the polymer with a higher density is pushed outward due to the centrifugal force while the monomer polymerizes thereby producing a graded concentration profile. Park et al.[23] introduced a coextrusion method using a specially designed coextrusion die which includes two rotating elements. In their method, two separate polymers with different refractive indices are introduced to the special die where a concentration gradient is created by spatial variation of the mixing ratio of the two input polymers.

2-2 Diffusion-Assisted Coextrusion Process

In this research, another method, which we will call *diffusion-assisted coextrusion process*, was developed and analyzed. In this process, core and cladding materials containing refractive-index-modifying additives are fed into a coextrusion die by two separate feeders that can be of any type such as extruders or gear pumps (Figure 2-1a). After a concentric core-cladding structure is formed in the coextrusion die, the materials proceed into a diffusion zone, where the additives diffuse from the core to the cladding or vice versa depending on which layer contains the additives. Since the material is solidified in a non-equilibrium state, a continuously varying additive concentration profile (or the refractive index profile) is created in the radial direction. The diffusion zone in this method is an extension of the coextrusion die where the outer surface of the cladding material is still in contact with the solid wall whose dimension can be varied to control the diffusional characteristics of the additives.

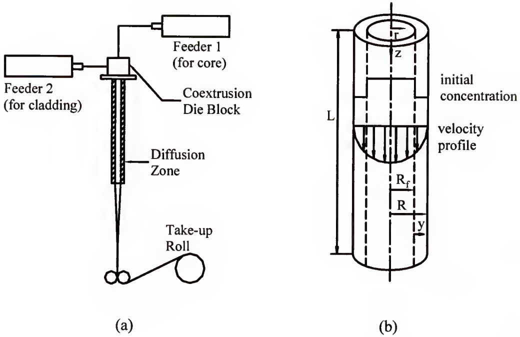

Figure 2-1. Diffusion-assisted coextrusion process
(a) Schematic diagram of diffusion-assisted coextrusion process.
(Feeders can be any types including extruders and gear pumps.)
(b) Schematic diagram of the concentric two-layer structure in the diffusion zone

This method is similar to the *closed extrusion process* developed by Ho et al.[24-28] In their process, polymer solutions in two different monomer mixtures are fed separately by gear pumps into a concentric (or coextrusion) die where a core-cladding structure of the two polymer solutions is formed. The concentric two-layered material then leaves the die and enters the enclosed zone while maintaining the two-layer structure in a solution state. In the enclosed zone where a constant temperature is maintained, the fiber surface is free (i.e., without contacting a solid surface) and mutual diffusion of the monomers in each layer takes place creating a refractive index profile. Subsequently, rapid reaction of the monomers is induced in the hardening zone by UV radiation forming a GRIN-POF.

Unlike the diffusion zone of the *diffusion-assisted coextrusion process*, the enclosed zone of Ho's process is a heating chamber where the fiber surface is free (i.e., contacts with a gas phase). Due to this difference, not only their processing characteristics are different, but also the materials that can be processed by each method are different. In this chapter, a theoretical analysis is provided for the diffusional characteristics of the additives in the *diffusion-assisted coextrusion process*. In addition, the bandwidth characteristics of the POF made by this process are also estimated by the *ray analysis*. As will be discussed later, the results indicate that it is difficult to obtain a near-parabolic refractive index profile by this method unless a very large residence time in the diffusion zone is provided. Nevertheless, a small variation of the refractive index in the radial direction created by the additive diffusion results in a significant increase in the bandwidth compared to that of the SI-POF suggesting that the *diffusion-assisted coextrusion process* is a viable method to fabricate a high bandwidth GRIN-POF although its refractive index profile may not be optimal.

2-2-1 Modeling

In this section, the additive concentration profile (hence the refractive index profile) created by the diffusion-assisted coextrusion process is estimated by solving the following convective diffusion equation:

$$\mathbf{u} \cdot \nabla x_{\mathrm{A}} - D_{\mathrm{A}} \nabla^2 x_{\mathrm{A}} = 0 \qquad (2\text{-}1)$$

Here **u** is the velocity field; x_{A} is the additive concentration profile, and D_{A} the diffusivity of the additive. Figure 2-1b indicates schematically the initial profile of the additive concentration and the velocity profile in the diffusion zone. Here we consider the case in which the core and cladding materials are the same, and only the core contains an additive. Poly(methyl methacrylate) (PMMA) containing benzyl butyl phthalate (BBP), benzyl benzoate (BEN) and diphenyl phthalate (DPP) is one of the most common materials used in the actual process.[15] These additives (i.e., BBP, BEN, DPP) have molecular weights in the range of 212 to 318, and are known to have good solubility in PMMA. The concentration of the additive may be in the range of about 10% by weight, which is large enough to alter the rheological properties of the core. For simplicity, however, it is assumed that the change in the rheological properties is negligible. In order to make an analytic progress, it is further assumed that the flow is axisymmetric and the fluids are Newtonian.

Under the prescribed assumptions, equation 2-1 gives the following dimensionless equation in a cylindrical coordinate system:

$$2\left(1-r^2\right)\frac{\partial x}{\partial z}=k^2\left(\varepsilon^2\frac{\partial^2 x}{\partial z^2}+\frac{\partial^2 x}{\partial r^2}+\frac{1}{r}\frac{\partial x}{\partial r}\right) \tag{2-2}$$

Here k^2 and ε are dimensionless parameters defined as $1/(\varepsilon^2 Pe)$ and R/L, and Pe is the Peclet number defined as UL/D_A. R and L are the radius and the length of the diffusion zone, and U is the average velocity of the material in the diffusion zone. The scalings for the nondimensionalization are R and L for the radial and the axial coordinate r and z, respectively. The velocity field $\mathbf{u}$ is scaled by U and the additive concentration x by the initial concentration in the core, x_o. Under the given assumption, the velocity field is parabolic.

Materials used in an actual process are not Newtonian. Consequently, the velocity profile is not parabolic. However, as it will be discussed later, the results obtained for a plug flow (i.e., equation 2-10) are not very much different from those for a parabolic flow. Therefore, it seems that the Newtonian assumption does not have a significant influence on the results of the present analysis.

Since the diffusion zone has a very large aspect ratio (i.e., $\varepsilon < O(10^{-2})$), the first term in the right hand side of equation 2-2 can be neglected to give

$$2(1-r)^2 \frac{\partial x}{\partial z} = k^2 \left(\frac{\partial^2 x}{\partial r^2} + \frac{1}{r} \frac{\partial x}{\partial r} \right) \tag{2-3}$$

The initial and boundary conditions are

$$\begin{aligned} x(r,0) &= 1 \quad \text{when } r \le R_f \\ x(r,0) &= 0 \quad \text{when } r > R_f \end{aligned} \tag{2-4}$$

$$\left. \frac{\partial x}{\partial r} \right|_{r=1} = 0 \tag{2-5}$$

$$\left. \frac{\partial x}{\partial r} \right|_{r=0} = 0 \tag{2-6}$$

Equation 2-4 indicates the step concentration profile at the inlet to the diffusion zone (i.e., at $z = 0$). R_f is the location of the interface between the core and the cladding, which can be varied by adjusting the flow rate ratio of the core and the cladding materials. Equations 2-5 and 2-6 are the no flux condition at the wall and the symmetry at the center, respectively.

Although this specific problem described by equations 2-3 through 2-6 has not been studied previously to our knowledge, classical problems tackled by Graetz[29] and Siegel et al.[30] are similar to this problem. Graetz analyzed a heat transfer problem in which a fluid with a constant temperature flows through a circular conduit with a constant wall temperature. Siegel et al. extended the Graetz problem to a case in which the heat flux at the wall was fixed. Following the similar procedure as Graetz, solution to the prescribed problem can be determined as

$$x = 2R_{\mathrm{f}}^{2}\left(1-\frac{R_{\mathrm{f}}^{2}}{2}\right)+\sum_{n=1}^{\infty}\frac{2}{\beta_n}\frac{R_f\left(\frac{dF_n}{dr}\right)_{r=R_f}}{\left[R_n\frac{\partial}{\partial r}\left(\frac{\partial F}{\partial \beta}\right)_n\right]_{r=1}}e^{-\frac{\beta_n^{2}}{2}k^{2}z}F_n(r,\beta) \qquad (2\text{-}7)$$

Here F_n is the eigenfunction corresponding to the eigenvalue β_n. Details of the solution procedure are given in Appendix A.

2-2-2 Simulation Results and Discussion

The additive concentration profile described by equation 2-7 has been plotted in Figure 2-2 for several different cases. The additive concentration profiles are directly related to the refractive index profiles since the refractive index of a mixture is given by the Lorentz-Lorenz equation[14]:

$$n = \sqrt{\frac{1+2\phi}{1-\phi}} \qquad (2\text{-}8)$$

where

$$\phi = \frac{\sum_i \frac{\left(n_i^{2}-1\right)x_i}{\left(n_i^{2}+2\right)\rho_i}}{\sum_i \frac{x_i}{\rho_i}} \qquad (2\text{-}9)$$

Here n_i, x_i and ρ_i are the refractive index, mass fraction, and the density of each component, respectively. This relationship is shown nearly linear unless the density difference between the mixture components is large. Thus, the concentration profiles given in Figure 2-2 should match closely to the refractive index profiles for most cases of our interest.

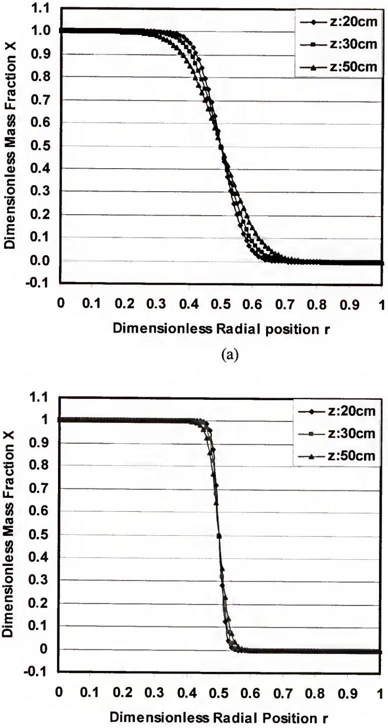

(a)

(b)

Figure 2-2. Additive concentration profiles at various axial positions ($R = 0.384$ cm, $R_f = 0.5$, $Q = 100$ g/hr).
(a) $D_A = 10^{-6}$ cm^2/s (b) $D_A = 10^{-7}$ cm^2/s.

In Figures 2-2a, b, the concentration profiles at three different axial positions are shown when the diffusivity of the additive is 10^{-6} and 10^{-7} cm^2/s, respectively. The position of the core-cladding interface is in the middle of the fiber radius (i.e., $R_f = 0.5$) for both figures. These values for the diffusivity have been chosen as they represent those of additives with the molecular weight of about 500 in a PMMA or polystyrene (PS) matrix at 200 ~ 230 °C.[16-17] When the diffusivity is 10^{-7} cm^2/s (Figure 2-2b), only a small change occurs in the concentration profile. When it is 10^{-6} cm^2/s (Figure 2-2a), on the other hand, the change is more significant. In all these cases, however, the additive concentration is rather uniform for a large part of the core (i.e., when r/R is smaller than about 0.3.). Therefore, a very large bandwidth that can be obtained with the optimum

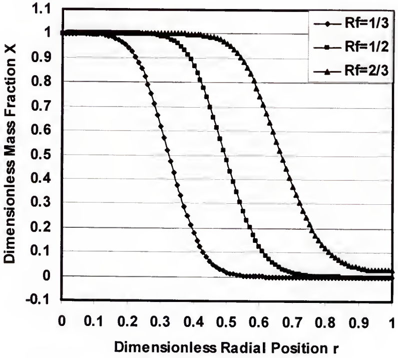

Figure 2-3 Additive concentration profiles at various values of R_f ($k^2 = 6.73\times10^{-3}$, $R = 0.384$ cm, $Q = 100$ g/hr, $D_A = 10^{-6}$ cm^2/s, $z = 50$ cm)

parabolic profile is not expected. Nevertheless, as it will be shown in the subsequent sections, the small change in the concentration profile results in a substantial increase in the bandwidth compared to that of the step-index profile. In addition, the smoothening of the refractive index profile is expected to improve attenuation of the optical fiber, since the sharp interface between the core and the cladding of SI-POFs is often a source of significant scattering loss of light signals due to surface irregularities.

In Figure 2-3, concentration profiles at $z = 50$ cm are shown for various values of the core-cladding interface position. Although the differences are not very large, the diffusion of the additive occurs to a greater extent when the interface position is farther away from the center axis (i.e., for a larger value of R_f). It is due to the larger interface

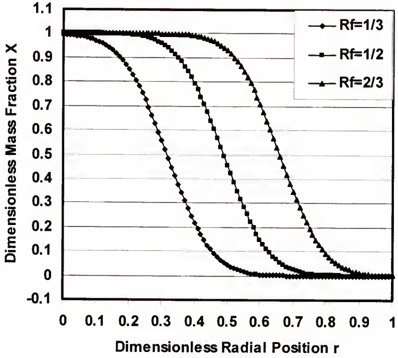

Figure 2-4 Concentration profiles for the closed extrusion process
($k^2 = 6.73\times10^{-3}$, $R = 0.384$ cm, $Q = 100$ g/hr, $D_A = 10^{-6}$ cm^2/s, $z = 50$ cm)

area through which the diffusion is taking place. In addition, the lower velocity near the outer radius of the die, which makes the material residence time larger, may also contribute to this enhanced diffusion.

As was described in the previous section, some similarities exist between the diffusion-assisted coextrusion process and the *closed coextrusion process* of Ho et al. from a process modeling point of view although they are significantly different from a processing viewpoint. Since the outer surface of the concentric two-layer material (or fiber) in the enclosed zone of the closed extrusion process is a free surface without any contact with a solid wall, the flow in this region is a plug flow. Thus, the convective diffusion process can be described by the same set of equations as equations 2-2 through 2-6 with the velocity field in equation 2-1 replaced by 1. In this case, the solution for the concentration profile is given by the Bessel functions of the first kind of orders 0 and 1 as follows:

$$x = R_{\mathrm{f}}^{\,2} + 2R_{\mathrm{f}} \sum_{m=1}^{\infty} \frac{J_1(\beta_m R_{\mathrm{f}})}{\beta_m J_0^{\,2}(\beta_m)} e^{-\beta_m^{\,2} k^2 z} J_0(\beta_m r) \tag{2-10}$$

Here J_0 and J_1 are the Bessel functions of the first kind of order 0 and 1, respectively. In Figure 2-4, three concentration profiles described by equation 2-10 under the same processing conditions as those for Figure 2-3 are given for comparison. It appears that the diffusion takes place to a slightly greater extent in the plug-flow situation than in the parabolic flow situation. It is probably due to the shorter contact time between the core and the cladding materials in case of the parabolic flow. Although the average velocity (hence the average residence time) is set to be the same for both processes, the local velocity of the core material is higher than that of the cladding in the parabolic flow.

Consequently, the net contact time between the neighboring fluid elements across the core-cladding interface is shorter decreasing the extent of diffusion.

The additive flux q at the interface position R_f in the radial direction is given by

$$q\Big|_{r=R_f} = -D_A \frac{\partial x_A}{\partial \tilde{r}}\Big|_{r=R_f} = -D_A \frac{x_0}{R}\frac{\partial x}{\partial r}\Big|_{r=R_f} \tag{2-11}$$

where $\tilde{r}$ is the dimensional radial position, and x_0 is the initial concentration of the additive in the core. Plugging the equation 2-10 into equation 2-11 gives us the additive flux in a plug flow case as

$$q\Big|_{r=R_f} = 2D_A x_0 \frac{R_f}{R}\sum_{m=1}^{\infty}\frac{J_1^{\,2}(\beta_m R_f)}{J_0^{\,2}(\beta_m)} e^{-\beta_m{}^2 k^2 z} \tag{2-12}$$

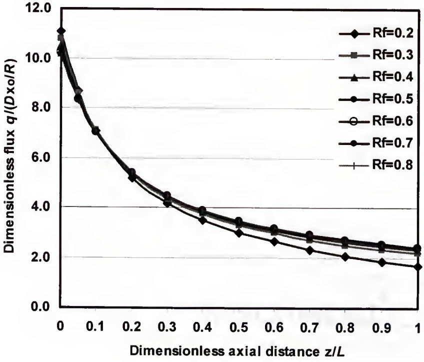

Figure 2-5 Dimensionless additive flux at the core-cladding interface ($k^2 = 0.013$, $R = 0.384$ cm, $Q = 100$ g/hr, $D_A = 10^{-6}$ cm^2/s, $z = 100$ cm)

The equation 2-12 also provides the net effect of the core-cladding interface position on the additive flux and the concentration profile regardless of the flow types, excluding the residence time effect due to the nonuniform velocity profile appearing in the tubular flow case. In figure 2-5, the normalized fluxes of the additive in the radial direction at the interface positions R_f are plotted for various R_f values. The flux increases with the interface position R_f although the initial flux at the inlet to the diffusion zone is greater when R_f is smaller.

2-2-3 Multi-layer Fibers

As Figures 2-2, 2-3 and 2-4 indicates, the variation of the additive concentration (or the refractive index) in the radial direction is restricted to the region near the core-cladding interface unless the material residence time is very large. This limitation in controlling the concentration profile may be overcome by adopting a multi-layer process.

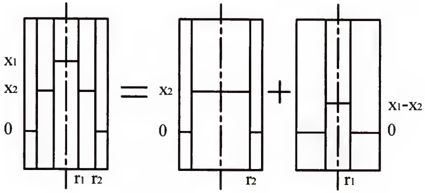

(a) (b) (c)

Figure 2-6 A three-layer diffusion process equivalent to the addition of two two-layer processes. (x_1 and x_2: initial concentration of the additive in the core (or 1st) and the 2nd layer, respectively.)

Since the governing equation for the convective diffusion is linear, the multi-layer diffusion problem can be described as an addition of several two-layer problems. Figure 2-6 shows schematically that the three-layer diffusion problem is equivalent to the addition of two two-layer problems. In other words, the solution to the problem described by Figure 2-6a is simply the summation of the solutions for Figure 2-6b and 2-6c. Consequently, the solution to a multi-layer problem can be obtained following the same procedure described in the Appendix section. As an example, concentration profiles obtained by a three-layer diffusion-assisted coextrusion process are shown in Figure 2-7. Obviously, the concentration profiles for three-layered fibers show more significant variation in the radial direction than two-layered fibers for the same operating

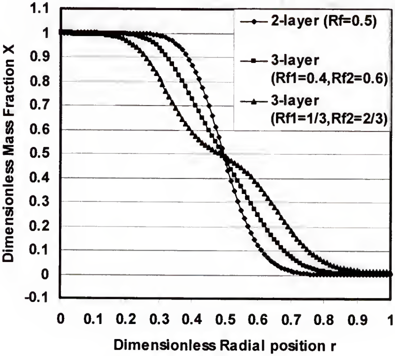

Figure 2-7 Additive concentration profiles of 2- and 3-layer fibers
($k^2 = 6.73\times10^{-3}$, $R = 0.384$ cm, Q = 100 g/hr, $D_A = 10^{-6}$ cm^2/s, $z = 50$ cm)

conditions. In principle, the concentration profile can be manipulated to match it closely to the ideal parabolic profile by multi-layer process.

2-3 Estimation of Bandwidth

In this section, the bandwidth characteristics of the fibers having refractive index profiles obtained from the simulation are estimated by the ray analysis.

The bandwidth of a GRIN fiber with its refractive index profile following the power law can be estimated by WKB (Wentzel, Kramers, and Brillouin) approximation.[31] When the refractive index profile is given by a rather complicated form as in equation 2-7 or 2-10, a simple analytic expression for the bandwidth is not available. While several different approaches may be applied for the estimation of the bandwidth, we have adopted the ray analysis for its simplicity.

2-3-1 Ray Optical Formulation of Impulse Response Function

In ray optics, estimation of the modal dispersion can be achieved by calculating the net travel time and transmitted power of each packet of rays following its propagation path from inlet to the outlet. The bounded rays follow a periodic path within the fiber core as shown in Figure 1-4, and the ray transit time over an axial distance *z* for a given value of κ and l is given as[32]

$$\tau = \frac{2z}{cz_p} \int_{r_{ic}}^{r_{tp}} \frac{n^2(r)}{\sqrt{g(r)}} dr \qquad \text{where} \quad g(r) = n^2(r) - \kappa^2 - l^2/(r/R)^2 \tag{2-13}$$

Here c is the speed of light in vacuum and z_p is the axial half period, which is given as

$$z_p = 2\kappa \int_{r_{ic}}^{r_{tp}} \sqrt{g(r)} dr \tag{2-14}$$

The integration limits r_{ic} and r_{tp} are the radii of so-called *inner caustic* and *turning point caustic*, respectively, between which the ray path is bounded (Figure 1-4). These caustics are zeros of the function $g(r)$ (i.e., $g(r_{ic}) = 0$ and $g(r_{tp}) = 0$).

For a uniform Lambertian source (Figure 2-8), which is the most typical source in practice and approximates the output of a light emitting diode (LED), the intensity distribution of input light is given as[5]

$$I = I_0 \cos\theta \tag{2-15}$$

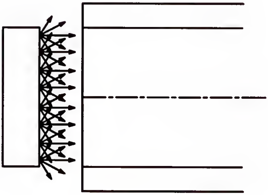

Figure 2-8 Schematic of a Lambertian light source.
The light intensity is independent of radial position, and is only dependent on the output angle.

and the power transmitted by the rays having the values of the two invariants in the range of κ to $(\kappa + d\kappa)$ and l to $(l + dl)$ is

$$dP = P_0 z_p(\kappa, l) d\kappa dl \qquad \text{where} \quad P_0 = 4\pi R\, I_0 / {n_0}^2 \tag{2-16}$$

The transmitted power can also be expressed in terms of transit time to give impulse response function $Q(\tau)$ as follows

$$dP = Q(\tau) d\tau \tag{2-17}$$

Following the approach of Barrell and Pask,[32] we discretized $\kappa - l$ domain into finite number of subdomains, and by calculating the transit time and the transmitted power in each subdomain, the impulse response curves for various refractive index profiles were obtained. The bandwidth was then calculated as the inverse of four times the standard deviation of the impulse response curve. The refractive index profiles were obtained from the concentration profiles in section 2-2 using equations 2-8 and 2-9 for 101 radial positions. The integrations of equations 2-13 and 2-14 were carried out analytically by setting the refractive index profiles as quadratic functions as in equation 2-18. This quadratic approximation of the refractive index profiles facilitates the calculation procedures since all the refractive index terms in equations 2-13 and 2-14 are expressed as quadratic or square root forms, and it also approximates the refractive index profiles produced by the diffusion-assisted coextrusion process very well.

$$n^2(r) = A + B\left(r/R\right)^2 \tag{2-18}$$

In Figure 2-9, various refractive index profiles are given for which the bandwidth has been estimated by the prescribed ray analysis. The profiles with locally graded-index (i.e., e, f and g in Figure 2-9) are the ones described previously in Figure 2-6. In calculating the bandwidth, we divided $\kappa - l$ domain into 1000 by 500 subdomains and considered the case for which $n_1 = 1.515$ and $n_2 = 1.498$; hence the numerical aperture (NA) is equal to 0.226.

The impulse response or the bandwidth of POFs is also affected by other factors such as material dispersion, mode coupling and differential mode attenuation (DMA).[33-35] The material dispersion is caused by a finite distribution of the wavelength of the incident light and the wavelength dependence of the refractive index of a material. Since non-

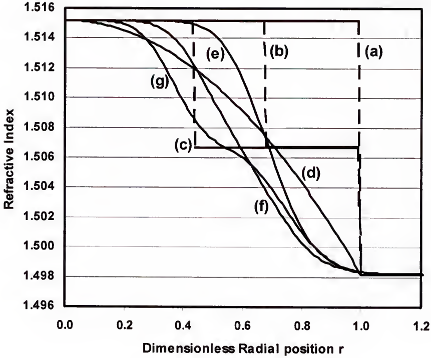

Figure 2-9 Refractive index profiles of multi-layered and GRIN fibers
(a) 2-layer step-index (b) 3-layer step-index ($R_f = 0.4, 0.6$)
(c) 3-layer step-index ($R_f = 0.3, 0.7$) (d) ideal graded-index ($\alpha = 2.0$)
(e) diffusion-assisted 2-layer (f) diffusion-assisted 3-layer ($R_f = 0.4, 0.6$)
(g) diffusion-assisted 3-layer ($R_f = 0.3, 0.7$).

ideal incident light always has a wavelength distribution, the material dispersion occurs unless the material is non-dispersive. However, it is reported to be small compared to the modal dispersion by orders of magnitude unless the modal dispersion is extremely small as in the single mode fibers. Since the input signal may not have uniformly distributed modes, differential mode attenuation (DMA) has an influence on the bandwidth of the optical fiber. In addition, mode coupling between higher and lower modes is known to have influence on the bandwidth characteristics.[33] Mode coupling, however, is shown to be negligible unless fiber length is longer than 100 m, and DMA apparently acts in a way to increase the bandwidth of POF.[34] Thus, the current analysis, in which the material dispersion, DMA and the mode coupling have not been considered, may provide the lower limit of the bandwidth.

2-3-2 Impulse Response Curves and Bandwidths

The impulse responses of the optical fibers with refractive index profiles given in Figure 2-9 are shown in Figure 2-10 and 2-11 as plots of normalized intensity versus transit time for a length of 1 m. The bandwidth for a 100 m fiber calculated as the inverse of 400 times the rms width of the impulse response (i.e., $1/400\sigma$) is shown in Table 2-1 for each optical fiber. The impulse response of the SI fiber (Figure 2-10a) shows a rectangular shape with the power equally distributed over minimum and maximum transit times. The bandwidth of the SI fiber is calculated to be 154 MHz (megabits per second), which is consistent with the result of the WKB approximation.

As the number of layers in multi-layer step-index fibers increases, the response curve (Figures 2-10b, c and d) becomes narrower and the mean transit time shifts toward a lower value approaching the delta function for an ideal GRIN fiber with $\alpha = 2$ (Figure 2-10e). The bandwidth of these multi-layered fibers increases almost linearly as the number of layers increases, and reaches about 400 MHz per 100 m when the number of layer is increased to nine (Figure 2-10d). Theses results are expected since a GRIN fiber may be considered as an extreme case of the multi-layered fiber with infinite number of layers.

When the sharp interfaces of the multi-layered step-index fibers are smoothened by the diffusion-assisted coextrusion process, the increase in bandwidth is quite significant. In figure 2-11, the response curves for the fibers whose interfaces are smoothened by the additive diffusion as in Figure 2-9e, f and g are shown. The response curves for those with sharp interfaces are overlaid as dashed lines for comparison.

When the sharp interface of the SI fiber is smoothened by the additive diffusion, the transmitted power at longer transit times becomes smaller and its bandwidth is more than doubled to 319 MHz per 100 m (Table 2-1).

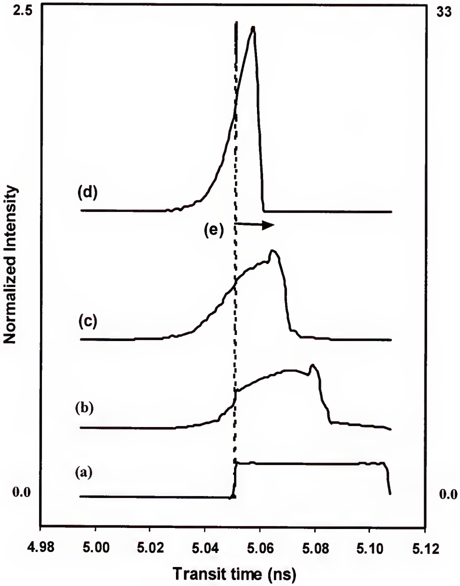

Figure 2-10 Impulse responses for 1 m long multi-layered fibers
(a) 2-layer SI (b) 3-layer SI (c) 4-layer SI (d) 9-layer SI (e) GRIN fiber

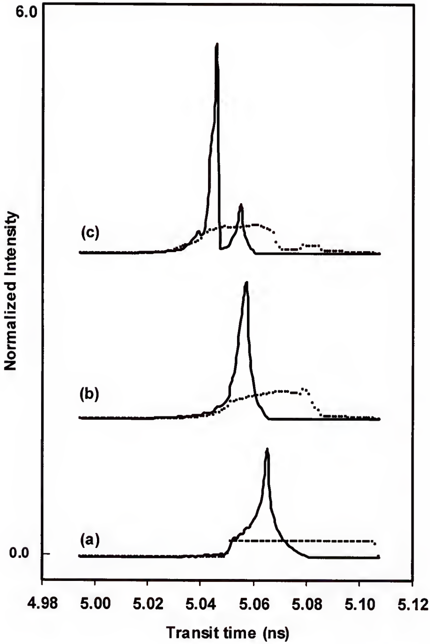

Figure 2-11 Impulse responses for 1 m long multi-layered fibers
(a) 2-layer ($R_f = 0.5$) (b) 3-layer ($R_f = 0.4, 0.6$) (c) 3-layer ($R_f = 0.3, 0.7$).
(Solid lines: smoothened interfaces, dashed lines: sharp interfaces)

Considering a rather small change in the refractive index profile, this large increase in the bandwidth may have a significant implication. As Table 2-1 indicates, bandwidth higher than 400 MHz per 100 m with numerical aperture 0.226 is obtainable only with three layers when diffusion-assisted extrusion process is applied, which otherwise requires nine layer step-index fiber with sharp interfaces. As indicated in Figures 2-9e and 2-9f, the refractive index profile can take on various shapes depending of the processing conditions, which in turn results in different impulse responses (Figures 2-11b and 2-11c) and bandwidths. Thus, further optimization of the refractive index profile is required to maximize the bandwidth.

Table 2-1 Bandwidth obtained by the ray analysis for various optical fibers described in Figure 2-9 (n_1 = 1.515, n_2 = 1.498; NA = 0.226). The impulse response curves are given in Figure 10 and 11.

Optical Fiber	Bandwidth (MHz per100 m)
2-layer SI fiber (Figure 2-9a)	154
3-layer SI fiber (sharp interfaces, Figure 2-9b)	200
3-layer SI fiber (sharp interfaces, Figure 2-9c)	180
4 layer SI fiber (sharp interfaces)	242
6 layer SI fiber (sharp interfaces)	327
9-layer SI fiber (sharp interfaces)	415
GRIN fiber (α= 2.0, Figure 2-9d)	26890
Diffusion-assisted 2-layer fiber (Figure 2-9e)	319
Diffusion-assisted 3-layer fiber (Figure 2-9f)	369
Diffusion-assisted 3-layer fiber (Figure 2-9g)	413

2-3-3 WKB Approximation

The WKB method is an approximation technique commonly used in quantum mechanics, and has often been used in optics, especially in dealing with GRIN fibers.

The bandwidth of a GRIN fiber with its refractive index profile following the power law can be estimated by WKB (Wentzel, Kramers, and Brillouin) approximation.[31] For the GRIN fiber with the refractive index profile described by equation 1-17, the rms width σ of the output signal is given by the following analytic expression

$$\sigma = \frac{Ln_1\Delta}{2c}\frac{\alpha}{\alpha+1}\left(\frac{\alpha+2}{3\alpha+2}\right)^{1/2}\left[C_1^{\,2} + \frac{4C_1C_2\Delta(\alpha+1)}{2\alpha+1} + \frac{4\Delta^2 C_2^{\,2}(2\alpha+2)^2}{(5\alpha+2)(3\alpha+2)}\right]^{1/2} \tag{2-19}$$

where

$$C_1 = \frac{\alpha-2-\varepsilon}{\alpha+2}\ ,\quad C_2 = \frac{3\alpha-2-2\varepsilon}{2(\alpha+2)}\ ,\quad \varepsilon = \frac{-2n_1\lambda\Delta'}{N_1\Delta}\ ,\quad N_1 = n_1 - \lambda\frac{dn_1}{d\lambda} \tag{2-20}$$

Here, c and λ are the speed and the wavelength of the light, and L the length of the optical fiber. Δ is given by equation 1-19, and Δ' denotes the derivative with respect to λ. This solution is based on the wave equation described in Chapter 1, and it is known that WKB approximation has almost the same accuracy as geometric optical analysis in predicting the intermodal dispersion of a GRIN fiber.[36]

In Figure 2-12, the bandwidth calculated by the ray analysis for GRIN fibers following the power-law with various values of the power-law index is compared with the results of the WKB approximation as a measure of accuracy for the present ray analysis. The bandwidth calculated by the ray analysis matches well with that obtained by the WKB method supporting the reliability of the present calculations.

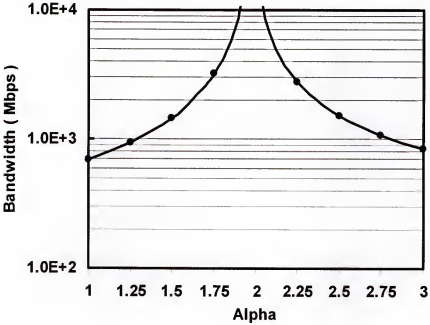

Figure 2-12 Comparison of bandwidths from ray analysis and WKB approximation for a 100 m GRIN fiber with various values of power-law index alpha. (line: WKB approximation, points: ray analysis)

2-4 Summary

The *diffusion-assisted coextrusion process* has been introduced as another method to fabricate graded-index plastic optical fibers. In this process, two or more polymeric materials containing refractive-index-modifying additives are fed separately into a coextrusion die where a concentric multi-layer structure is formed. The multi-layered materials then proceed into a diffusion zone, where the additives diffuse forming a desired concentration (or refractive index) profile.

Theoretical analysis for the refractive index profile indicates that it is difficult to obtain a near-parabolic refractive index profile by this method unless a very large residence time in the diffusion zone is provided. However, the refractive index profile can be altered significantly by adopting multi-layer approach. Furthermore, the bandwidth estimated by the ray analysis indicates that a small variation of the refractive index profile created by the additive diffusion can result in a significant increase in the bandwidth compared to that of the SI-POF with sharp interfaces. Present results suggest that the *diffusion-assisted coextrusion process* is a viable method to fabricate GRIN-POFs with bandwidth higher than 400 MHz per 100 m with numerical aperture 0.226.

CHAPTER 3
FABRICATION AND CHARACTERIZATION OF GRIN POF

In this chapter, experiment is described in which PMMA base GRIN POFs were prepared by the diffusion-assisted coextrusion process that was analyzed in Chapter 2 in detail. Measured refractive index profiles are also described as well as the bandwidth characteristics estimated by the ray analysis.

3-1 Preparation of GRIN Fibers

Two additives were used to investigate the effectiveness of this process for fabricating GRIN POFs. One is Oil Red EGN (MW 418) whose molecular structure is shown in Figure 3-1a. This red pigment was adopted due to its good compatibility with poly(methyl methacrylate) (PMMA), and it was used for visualization of concentration profiles in a GRIN fiber and demonstration of the effect of the additives' diffusivities on the final concentration profiles.

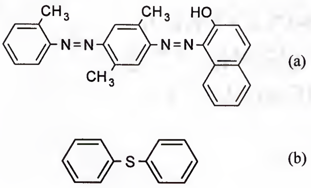

Figure 3-1 Molecular structures of
(a) Oil Red EGN and (b) DPS

The other additive, DPS (Diphenyl sulfide, MW186) (Figure 3-1b) was used as refractive-index modifying dopant. It has much higher refractive index (1.633) than PMMA (1.491), which enables us to minimize the amount of additive in the GRIN POF maintaining high numerical aperture. It is desirable to keep the dopant level as low as possible because the small molecules used for dopants not only act as plasticizers and decrease the maximum service temperature of the GRIN POF, but also increase the scattering losses of the fiber.

Diphenyl sulfide is known to be compatible with PMMA, and has high enough diffusivity at process temperatures (180 to 220 °C) to produce smooth GRIN profiles as will be shown later in this chapter. It also has very good thermal stability at elevated temperatures. Thermal stability of GRIN POFs is an important issue since its profile is subject to degradation upon long-term usage, especially at elevated temperatures, resulting in deterioration of its performance. Sato et al.[37] has reported that the thermal stability of refractive indices is affected by diffusivity and plasticization effect of dopant material, and materials with high polar groups attached to aromatic rings are the best candidates for the dopant with low plasticization effect. In their study, PMMA-base GRIN POF with DPS as dopant prepared by interfacial gel polymerization showed little change in refractive index profile or in bandwidth characteristics after 12000 hours of aging at 85 °C.

3-1-1 DPS-Doped GRIN Fibers

First, additive master batches, mixtures of polymer with additive material, were prepared by the following procedures. 106.6 g PMMA (Rohm&Haas Plexiglas H-15) was dissolved in 212 mL toluene, then 26.9 g DPS (Fluka) was added into the PMMA solution followed by 3 hours of mixing. The resulting solution was cast into sheets and dried under vacuum increasing temperature from 25 to 70 °C for 7 days. The dried sheet was pelletized to the size of original PMMA chips (i.e., about 3 mm) and stored in vacuum for the subsequent extrusion experiments. DPS concentration in the final master batch chips prepared thereby were 20 wt %.

The master batches prepared by prescribed methods and pure PMMA were extruded using two ¾″ extruders. Although we used two extruders for the feeding of the raw material, the feeders can be any types including gear pumps or hydraulic pumps. The core layer contained 32.5 wt % master batches with 67.5 wt % pure PMMA, resulting in 6.5 wt % DPS in the core layer, while the cladding layer was pure PMMA.

It has been known that PMMA is highly hygroscopic and absorbs moisture up to 0.6 wt % at room temperature,[38] which may cause lots of bubbles when extruded at high temperatures. To avoid bubbles, raw materials were dried under vacuum at 70 °C for at least 24 hours prior to extrusion. After passing though the coextrusion die, the concentric melt entered a 7.67 mm wide, 50 cm long heated tube to produce concentration gradient of the additive by molecular diffusion across the core-cladding interface of the fiber. The fiber coming out of the heated tube was cut and quenched in cool water bath for the refractive index characterization. The diameter of the final fiber was about 3 mm. The flow rate range investigated was 74.5 to 87 g/hr with average residence time in the tube of 18.6 to 21.5 minutes, and the melt temperatures in the diffusion zone were 188 to 216 °C.

The concentration profiles of DPS in the fiber (and refractive index profiles) fabricated thereby were measured by FT-IR spectroscopy. Thin cross-sectional fiber samples were prepared and scanned across the radius by the following procedures. First, the fibers were sliced into 1 mm thick disks, and ground with abrasive papers (grit numbers 400 and 2000 successively). The remaining fine scratches on the surfaces of the disks, which would cause scattering of light at the surface, were removed by polishing with Al_2O_3 slurry (Alfa, 20% aqueous, average particle size 50 nm, pH 4). They were then washed in deionized water and dried in vacuum to make 100 μm thick samples.

Samples prepared thereby were placed on a gold mirror under a microscope attached to Nicolet Magna FT-IR 760, and focused light from Nernst glower through 10× object lens was lit on the sample. Part of the light incident on the sample is reflected from the sample surface and the light passing through the surface is either absorbed or reflected at the interface of the sample and mirror. This reflected light again experiences multiple reflections and absorptions within the sample until it passes through the sample surface or fully absorbed by the sample. The light coming out of the surface was detected by an MCT detector. One hundred and twenty eight spectra with the spectral range of 4000 – 650 cm^{-1} were collected for every 50 μm radial position and averaged.

The relationship between additive concentration and transmitted light can be obtained from Beer's law (abc rule):[39]

$$A \equiv \log(I_0/I) = abc \tag{3-1}$$

Here A is the absorbance defined as logarithm of the ratio of the incident and transmitted light intensities, a is the absorptivity or extinction coefficient, b is the path length of the sample, and c is the concentration of additive in gram per liter. The concentration of the additive at each radial position was obtained from the absorbance spectra using the above equation because it is directly proportional to absorbance.

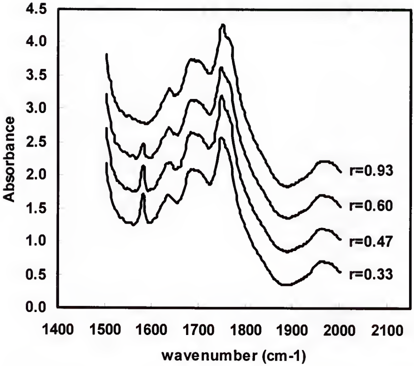

Figure 3-2 FT-IR spectra of DPS-doped GRIN fiber at four different radial positions (R = 0.384 cm, Q = 100g/hr, z = 50 cm, melt temperature: 188 °C, k^2=0.0037).

In Figure 3-2, FT-IR spectra of the DPS-doped fiber at four different radial positions are plotted. The peaks appearing at 1581 cm^{-1} are characteristics of the phenyl groups in the DPS molecules, and those at 1749 cm^{-1} are for the ester groups in the PMMA molecules.

It should be noted that the peak of the phenyl group gets smaller with radial position of the fiber, while ester peak shows little variation. The height of each phenyl peak was measured and normalized by the corresponding ester peak, and the concentrations of DPS in the fiber calculated using Beer's law were plotted in Figure 3-3. Flow rates investigated were 74.5, 80.9, 80.7 g/hr with the average residence times in the diffusion

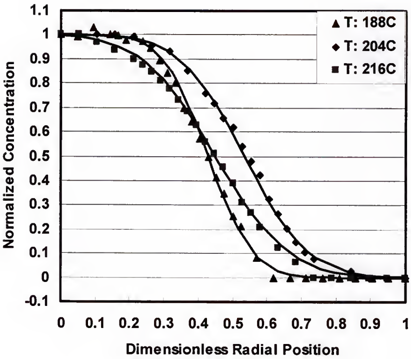

Figure 3-3 Concentration profiles of DPS in DPS-doped GRIN fibers (Dots: measured, line: calculated, $R = 0.384$ cm, $z = 50$ cm,
$Q = 74.5$ g/hr, $D_A = 1.01\times10^{-6}$ cm^2/s for melt temperature 188 °C, $k^2 = 0.0037$
$Q = 80.9$ g/hr, $D_A = 1.95\times10^{-6}$ cm^2/s for melt temperature 204 °C, $k^2 = 0.01$
$Q = 80.7$ g/hr, $D_A = 2.85\times10^{-6}$ cm^2/s for melt temperature 216 °C, $k^2 = 0.02$).

zone of 21.5, 19.7, 19.8 minutes, and the interface position R_f were 0.43, 0.60, 0.45 for the melt temperature at the diffusion zone 188, 204, 216 °C respectively.

The concentration profiles clearly show the additive diffusion across the core-cladding interface. Although the variation of the additive concentration (or the refractive index) in the radial direction is restricted to the region near the core-cladding interface when the melt temperature is 188 °C, it increases considerably with the melt temperature. When the melt temperature is 216 °C, the profile shows quite a slant shape, opening possibilities of obtaining high bandwidths with near-parabolic refractive index profiles.

This significant increase of additive diffusion with temperature in the polymer matrix is expected because temperature dependence of the diffusivity of small molecules follows Arrhenius law for a small temperature range as discussed later in this chapter.

As discussed in Chapter 2, the concentration profiles are controlled by the dimensionless parameter k^2, and the effect of increasing temperature (consequently increasing diffusivity of dopant molecules) is equivalent to increasing the residence time of the molecules in the diffusion zone since k^2 is directly proportional to diffusivity and residence time.

In addition, the diffusivity at each melt temperature was calculated from the measured concentration profile by applying the model described in Chapter 2. By minimizing the sum of the shortest distances between measured concentrations and the model curve from equation 2-7 with diffusivity as an adjustable parameter, the diffusivity at each temperature was estimated. The measured concentration profiles show relatively smooth profiles, and match quite well with the profiles calculated by the model equation with diffusivities 1.01, 1.95, 2.85×10^{-6} cm^2/s at 188, 204, 216 °C. Diffusivities estimated agree on the order of magnitudes with diffusivities of small molecules predicted by the free volume theory.[40-48]

3-1-2 Oil Red EGN-Doped GRIN Fibers

Master batch chips containing 0.465 wt % Oil Red EGN in PMMA prepared by the same procedures with DPS master batch, and pure PMMA were extruded. The core layer contains 5 wt % master batch with 95 wt % pure PMMA, and the cladding has only pure PMMA as in the case of DPS-doped GRIN fiber. The initial concentration of Oil Red

EGN in the core layer was 230 ppm, which was high enough to produce visible color gradient in the fiber and to be detected by UV spectrophotometry.

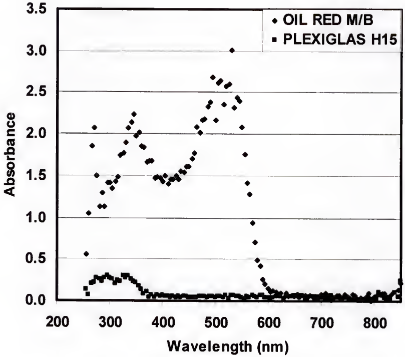

Figure 3-4 UV absorption spectra of Oil Red EGN 0.465 wt % containing PMMA and pure PMMA (Rohm & Haas Plexiglas H-15).

The concentration profiles of Oil Red EGN in the fiber were measured with Zeiss Axiotron Microscope spectrophotometer. With 100 μm thick cross sectional sample on a motorized stage, UV light from mercury lamp was focused with 20× object lens and lit to the sample, and the intensity of the transmitted light was detected with a PMT (photomultiplier tube). Because Oil Red EGN has the maximum UV absorption at 520 nm as shown in the Figure 3-4, 520 nm incident light with 20 nm spectral bandwidth was

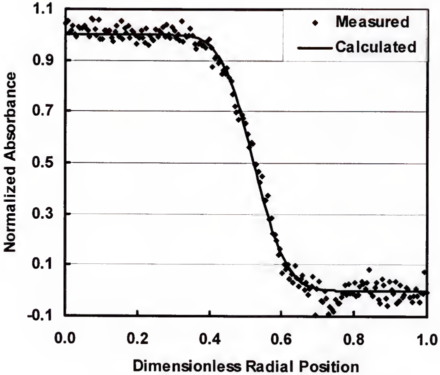
1.1
0.9
0.7
0.5
0.3
0.1
-0.1
Normalized Absorbance
0.0
0.2
0.4
0.6
0.8
1.0
Dimensionless Radial Position
Measured
Calculated

(a)

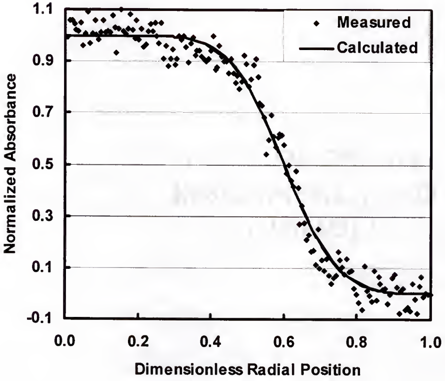
1.1
0.9
0.7
0.5
0.3
0.1
-0.1
Normalized Absorbance
0.0
0.2
0.4
0.6
0.8
1.0
Dimensionless Radial Position
Measured
Calculated

(b)

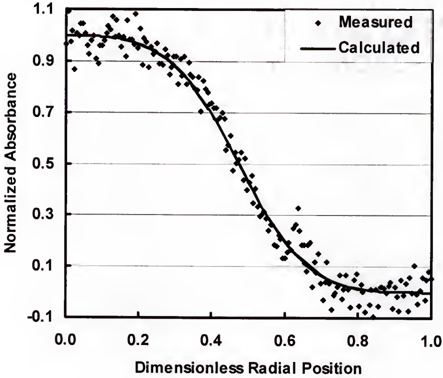

(c)

Figure 3-5 Concentration profiles of Oil Red EGN in Oil Red EGN-doped GRIN fibers (Dots: measured, line: calculated, $R = 0.384$ cm, $Q = 87$ g/hr, $z = 50$ cm)
melt temperature: 188 °C, $D_A = 4.90\times10^{-7}$ cm^2/s
melt temperature: 204 °C, $D_A = 1.17\times10^{-6}$ cm^2/s
melt temperature: 216 °C, $D_A = 2.30\times10^{-6}$ cm^2/s.

selected by passing the source light through a grating monochromator. The samples were radially scanned with a spatial resolution of 10 μm, and five scans for each sample were collected and averaged to reduce errors caused by source light fluctuation and detector noise.

In Figure 3-5, normalized absorbances of the Oil Red EGN-doped PMMA fiber were plotted against dimensionless radial positions of the fiber. The flow rate was 87 g/hr, average residence time in the diffusion zone was 18.6 minutes, and three different melt temperatures of 188, 194, and 216 °C in the diffusion zone were investigated. The initial core-cladding interfacial positions R_f were 0.526, 0.587 and 0.474 for Figures 6a, b and c, respectively. The diffusivities of Oil Red EGN in PMMA matrix were calculated following the same method as in DPS case, and found to be 4.9×10^{-7} cm^2/s, 1.17×10^{-6} cm^2/s and 2.3×10^{-6} cm^2/s at 188, 204 and 216 °C, respectively. The diffusivities of Oil RED EGN were appeared 0.5 to 0.75 times of those of DPS in the same PMMA matrix at the same temperatures. Therefore, Oil RED EGN-doped GRIN POFs have stiffer profiles at the same temperatures. Considering that the molecular weight of Oil Red EGN is 2.3 times of DPS, these diffusivity differences are expected because diffusivities are roughly proportional to inverse of the square root of molecular weight.[40]

3-2 Temperature Dependence of Diffusivity

Diffusion coefficients of small molecules in polymer matrix are typically in the range of 10^{-5} to 10^{-10} cm^2/s at 200-230 °C and are known to show Arrhenius-type temperature dependences[41]. One of the most successful theories on the diffusion of small molecules is the Cohen and Turnbull's free-volume theory, which correlates the diffusivity with the Maxwell distribution of the free hole volume and the molecular volume of solutes. Vrentas and Vrentas[42-48] were quite successful in expanding their theory to the molecular diffusion in polymeric matrices, and in the limit of low solute concentration above T_g, their results can be expressed in terms of WLF (Williams-Landel-Ferry) equation:[41]

$$\log a_T = \log\frac{D(T)}{D(T_g)} = \frac{C'_{1g}(T-T_g)}{C'_{2g}+T-T_g} \tag{3-2}$$

where a_T is the shift factor in the time-temperature superposition principle, and the coefficients C'_{1g} and C'_{2g} are related with the properties of polymer and solute by the following relations:

$$C'_{1g} = \xi \frac{\alpha_f B_0}{f_g \ln 10} \tag{3-3}$$

$$C'_{2g} = C_{2g} = \frac{f_g}{\alpha_f} \tag{3-4}$$

Here ξ is the ratio of critical molar volume of the solute jumping unit to the critical molar volume of the polymer matrix and related with the ratio of tracer and matrix molecular jumps size and shapes, α_f is the difference in expansion coefficient above and below T_g, and f_g is the fractional free volume at T_g, defined as the ratio of the average free volume over molecular volume.

According to Vrentas[47], if the solute jumps as a single unit, the parameter ξ can be estimated by the following relationship:

$$\xi = \frac{\xi_L}{1 + \xi_L (1 - A/B)} \tag{3-5}$$

and

$$\xi_L = \frac{\widetilde{v}_1^0(0)}{\widetilde{v}_2^*} \tag{3-6}$$

Here $\widetilde{v}_1^0(0)$ is the molar volume of the equilibrium liquid solute at 0 K, $\widetilde{v}_2^*$ is the critical hole free volume per mole of polymer jumping unit required for displacement of a penetrant jumping unit, and B/A is the aspect ratio of the penetrant molecule.

According to Bondi[49], zero point molar volume can be approximated by

$$\frac{\tilde{v}_1^0(0)}{\tilde{v}_w} \approx 1.3 \tag{3-7}$$

from the van der Waals volume $\tilde{v}_w$, and $\tilde{v}_2^*$ in equation 3-6 is given as 135 cm^3/mol for PMMA by Vrentas.[47]

Differentiating equation 3-2 gives us the temperature dependence of diffusivities by the following equation,

$$\frac{d\log D}{d(1/T)} = -\frac{C'_{1g}C'_{2g}T^2}{\left(C'_{2g}+T-T_g\right)^2} \tag{3-8}$$

Table 3-1. Free Volume parameters used for the estimation of temperature dependences of diffusivities of Oil Red EGN and DPS in PMMA matrix

α_f (K^{-1})	α_f/B (K^{-1})	f_g	T_g (K)	$\tilde{v}_2^*$ (cm^3/mole)
3.2×10^{-4}	6.3×10^{-4}	0.0168	378	135

Additive	$\tilde{v}_w$ (cm^3/mole)	A/B	ξ	C'_{1g}	C'_{2g}
Oil Red EGN	216.21	0.342	0.878	11.528	52.5
DPS	102.48	0.567	0.691	9.073	52.5

The free volume parameters used for the estimation of temperature dependences of diffusivities are listed in Table 3-1. The van der Waals volumes were obtained from the group contribution theory,[50-52] and the aspect ratios of the molecules were calculated as follows. First, the most stable conformation of a diffusive molecule were obtained by minimizing energy of the molecule with GAMESS (Ab initio computation software) in cooperation with Chem3D (CambrigdeSoft, Inc.), then two principal axes of that molecule were aligned with X and Y axes in Chem3D space. Length-to-breadth ratios were calculated by drawing rectangles that completely enclose the molecule with minimum areas in X-Y and X-Z plane following Rohrbaugh and Jurs's approach.[53] According to Berens and Hopfenberg,[54] the motion of small anisometric molecules through a polymer matrix occurs preferentially in a direction which minimizes the displacement required of the polymer chains; i.e., anisometric molecules, in fact, are oriented and move primarily along their long axes during diffusion through a polymer. They experimentally showed that diffusion of anisometric penetrants is governed by dimensions smaller than its equivalent spherical diameter. In this perspective, the aspect ratio of a molecule was calculated as the geometric mean of the two length-to-breadth ratios.

In Figure 3-4 are Arrhenius plots for the diffusivities of DPS and Oil Red EGN obtained from the curve fittings described in Section 3-1 and their linear regression lines, showing log(*D*) depends linearly on $1/T$ in this temperature range as expected. The slopes are –3.7 and –5.4 for DPS and Oil Red EGN, respectively, and calculated ones at 204°C by the prescribed method based on free volume theory were –3.65, –6.0. They agree pretty well, supporting reliability of diffusivity estimation of small molecules by this method.

In calculating the diffusivity of DPS, the glass transition temperature was taken to be different from that of pure polymer because of the plasticization effect of small molecules. The glass transition temperature of a polymer solution was estimated by[50]

$$T_g = \frac{T_{gp} + \left(KT_{gs} - T_{gp}\right)\phi_s}{1 + \left(K + 1\right)\phi_s} \tag{3-9}$$

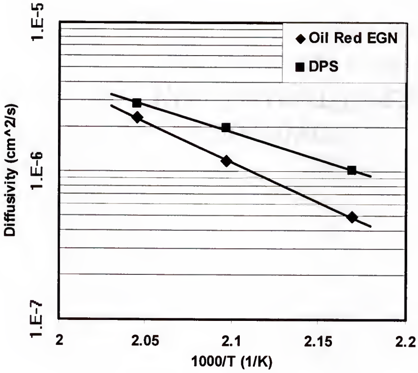

Figure 3- 4 Diffusivities of DPS and Oil Red EGN in PMMA matrix (Points: from curve fitting of measured concentration, lines: linear regression lines).

where subscripts *p* and *s* stand for polymer and solvent respectively, ϕ is volume fraction, and *K* is the ratio of the difference in thermal expansion coefficients of solvent above and below T_g to that of polymer:

$$K = \frac{\alpha_{ls} - \alpha_{gs}}{\alpha_{lp} - \alpha_{gp}} \qquad (3\text{-}10)$$

80 °C was used for the T_g of 6.5 wt % DPS-containing PMMA, and 105 °C for 230 ppm Oil Red EGN-containing PMMA.

3-3 Stability of Refractive Index Profiles

Since the GRIN POFs made with low molecular weight dopants are not in an equilibrium state, the refractive index profiles can change in long-term applications, and the stability of the refractive index profiles directly affects the numerical apertures and the bandwidth characteristics of the optical fibers.

Polymers with higher glass transition temperatures such as polycarbonates, polyimides or polysiloxanes are recently used in the high temperature applications. Flipsen et al.[55] introduced a multimode SI fiber based on crosslinked polysiloxanes, which can be used at relatively severe thermal conditions up to 200 °C. However, for the polymers mentioned above, it is difficult to obtain low optical losses due to their

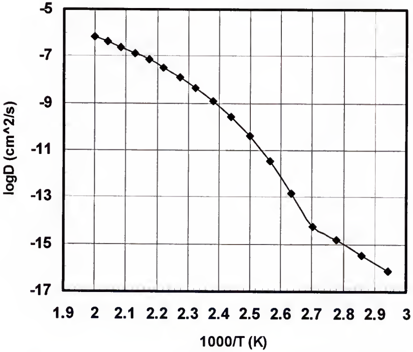

Figure 3-6 Diffusivity of TTI in PS predicted by free volume theory (MW of TTI 228, *Tg* of PS: 100 °C)

relatively high intrinsic molecular absorption, and hence their applications are limited for very short distances.

It has been verified through experiments that the kind of dopants and their concentrations in polymer matrix strongly influence the thermal stability of GRIN POF, especially the degradation of the refractive index profiles.[37] Obviously, the thermal stability of refractive indices is affected by diffusivity and plasticization effect of dopant material, and the stability as a function of time and temperature is predictable from the transport kinetics of the dopant molecules in polymer matrices.

Table 3-2. Free Volume parameters used for the estimation of temperature dependences of diffusivity of TTI in PS matrix

α_f (K^{-1})	α_f/B (K^{-1})	f_g	T_g (K)	$\tilde{v}_2^*$ (cm^3/mole)
3.7×10^{-4}	5.6×10^{-4}	0.021	373	135

Additive	$\tilde{v}_w$ (cm^3/mole)	A/B
TTI	136.82	0.57

In Figure 3-6, diffusivities of TTI (Tetrahydrotheophene-indigo, photochromic dye, mw 258) in polystyrene matrix at various temperatures calculated from the free volume theory as described in the previous section are plotted as an example. The free volume parameters used for the calculations were adopted from Ehlich and Sillescu[41], and listed in Table 3-2. The diffusivity increases linearly with temperature in the Arrhenius plot until the temperature reaches T_g, beyond which the diffusivity increases more rapidly. Therefore, there should be another coupling parameter λ in the equation 3-4 to describe the diffusivity in polymer matrix properly when the temperatures of observation spans from below to above T_g:

$$C'_{2g} = C_{2g}/\lambda \tag{3-11}$$

The second coupling parameter λ describes the change in the free volume expansion coefficient attributed to the onset of the glass transition. In other words, the mobility of the segment of polymer dramatically changes around T_g and enhance the molecular diffusion of the dopant molecules above T_g. The value of λ is equal to one above T_g, resulting $C'_{2g} = C_{2g}$ as in equation 3-4, and it is less than one below T_g.

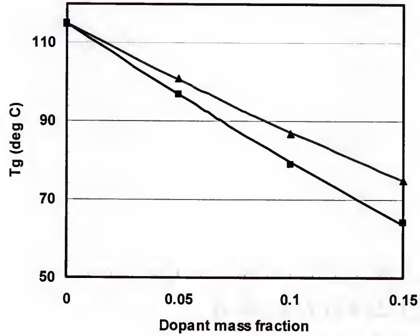

Figure 3-7 T_g behavior of DPS-PMMA and DPSO-PMMA mixtures (marks: measured[37], lines: curve fitting with K as adjustable parameter)

Thermal stability of POF and glass optical fiber is generally tested around 85 °C, which is one of the thermal stability standards of communication cables[15]. Therefore, it is important to keep the T_g of the polymer-dopant mixture above 85 °C to suppress the migration of dopant molecules due to their high diffusivity above T_g.

Figure 3-7 shows the behavior of the calculated T_g using equation 3-9 for DPS-PMMA and DPSO(Dipheny sulfoxide)-PMMA mixtures. The K values in the equation 3-9 were estimated by curve fitting of the experimental data of Sato et. al.[37] . As expected, DPS has slightly higher plasticization effect than DPSO, and about 5 wt % of DPS decreases T_g of PMMA by about 15 °C. To obtain highest possible numerical apertures keeping the lowest T_g of the fiber above 85 °C, 6.5 wt % of DPS and 7.5 wt % of DPSO were chosen for the experiments in Chapters 3 and 4. The dopants, 6.5 wt % of DPS and 7.5 wt % of DPSO in PMMA matrix lower the Tg's of PMMA from 115 °C to 94 and 92 °C, respectively, which are well above the standard test temperature.

3-4 Estimation of Bandwidth

In this section, impulse response curves were calculated and their bandwidths were estimated by ray analysis described in Chapter 2 for the fibers with refractive index profiles shown in Figure 3-3. As described in the previous chapter, light rays from an uniform Lambertain source was divided into 1000 times 500 subdomains in two invariants κ–l domain (equations 1-4 and 1-5), and transit time and power at the end of a fiber for each subdomain was calculated.

Impulse response curves for 1 m long fibers having refractive index profiles shown in Figure 3-3 are plotted in Figure 3-8 for which the maximum refractive index at center is 1.500 and the minimum index at the outer edge of the fiber is 1.491. The numerical aperture in this case is 0.164. As the melt temperature increases, the refractive index profile broadens getting closer to the parabolic shape, and the response curve gets sharper with a shift toward left as we pointed out in Chapter 2. Bandwidths estimated from the response curves as the inverse of 400 times rms width σ were 587, 670, and 616 MHz, which are much higher than those calculated from the virtual profiles in Chapter 2. This is because the bandwidth is strongly affected by numerical aperture of the fiber, and the numerical apertures of the index profiles in Chapter 2 were 0.226, which is 1.4 times larger than this case.

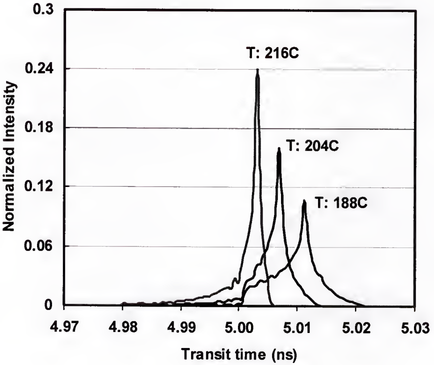

Figure 3-8 Impulse response curves for 1m long DPS-doped fibers, whose Refractive index profiles given I Figure 3-3.
(Numerical aperture: 0.164, refractive index at center: 1.500).

According to Arnaud,[56] the minimum rms width of an optical fiber with power-law index profile can be found at $\alpha = \alpha - 2.4\Delta$ as

$$\sigma_{\min} = 0.022 L N_1 \frac{\Delta^2}{c} \tag{3-12}$$

and the numerical aperture is related with Δ by

$$NA = n_1 \sqrt{2\Delta} \tag{3-13}$$

Hence, the bandwidth is proportional to $(NA)^{-4}$ for power law fibers.

Although the profiles used in this chapter can be approximated reasonably well by the power law in the region near the fiber axis where the profile curves show upper convex, they are significantly different from power law profiles in the overall sense.

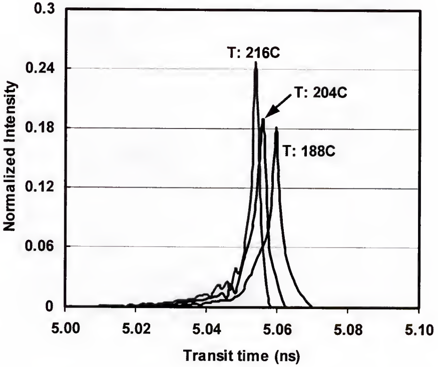

Figure 3-9 Impulse response curves for 1m long DPS-doped fibers (Numerical aperture: 0.226, refractive index at center: 1.5152).

Consequently, the numerical aperture dependence of bandwidth is smaller than power law fibers.

In Figure 3-9, impulse response curves for the fibers having the same dopant concentration profiles, but larger numerical aperture 0.226 are plotted for comparison. The widths of the curves are broadened with the shapes of the curves remained the same as the cases of NA = 0.164. Their bandwidths calculated were 356, 340 and 334 MHz for k^2 is 0.0037, 0.01, 0.02, respectively. Their bandwidths are only about half of those of the fibers with NA = 0.164.

It can be also noted in Figures 3-8 and 9 that the curves are significantly different from Gaussian with long tails in the short transit time region. Therefore, bandwidths calculated from the full width at half maximum (FWHM) may better predict the data transmitting capability of the fibers for the reasons mentioned in Chapter 1, and they are

Table 3-3 Bandwidths obtained from rms width and FWHM for various refractive index profiles

Refractive Index Profile		Bandwidth MHz per 100 m	
		From rms width	From FWHM
NA 0.164 (Figure 3-5)	Melt T: 188 °C (k^2 0.0037)	517	1757
	Melt T: 204 °C (k^2 0.01)	670	2287
	Melt T: 216 °C (k^2 0.02)	616	3637
NA 0.226 (Figure 3-7)	Melt T: 188 °C (k^2 0.0037)	356	1134
	Melt T: 204 °C (k^2 0.01)	340	1296
	Melt T: 216 °C (k^2 0.02)	334	1953

listed in Table 3-3. It is noteworthy that the bandwidths obtained from FWHM are much greater than those from rms width, and over 3 GHz is obtainable when the parameter k^2 is 0.02. The differences between two bandwidths calculated from two methods are due to the fact that most response curves have long tails in the low transit time region and very sharp peaks at the maximum height. Considering that the tails at the low transit region do not affect much on the bandwidth limit of a fiber since a certain amount of signal overlap is allowed in real data communication, bandwidths predicted from FWHM have more significant implication, and those from rms widths may be considered as lower bounds of the maximum obtainable bandwidths

3-5 Summary

Poly(methyl methacrylate)-base GRIN-POFs were successfully prepared by diffusion-assisted coextrusion process. Using DPS and Oil Red EGN as dopants, GRIN POFs were prepared by coextrusion followed by molecular diffusion varying operating conditions such as melt temperature and flow rates. Their concentration profiles, and refractive index profiles were characterized by FT-IR and UV spectroscopy, and compared with a theoretical model. The diffusivities of dopants were found to be 10^{-7}–10^{-6} cm^2/s range, which is consistent with the predictions from free volume theory. The concentration profiles are strongly affected by diffusivities of dopants, and can be controlled with the dimensionless parameter k^2 by changing processing temperatures and residence time because the diffusivities of the dopants in PMMA matrix follow Arrhenius type dependence on temperature.

The bandwidths of the GRIN POFs prepared thereby with numerical aperture 0.164 were estimated by ray analysis, and it was shown that bandwidth over 600 MHz per

100m could be obtained by this method, confirming the findings by theoretical analysis that the *diffusion-assisted coextrusion process* is a viable method to fabricate GRIN-POFs with high bandwidth.

CHAPTER 4
ANNULUS DIFFUSION SYSTEM

4-1 Introduction

In Chapter 2 and 3, it was shown that gradient index profiles can be effectively produced by the diffusion assisted coextrusion process. However, a relatively large residence time is needed to obtain a near-parabolic refractive index profile by two-layer coextrusion. It would be advantageous to obtain the same profile with less residence time not only for the productivity but also it will reduce contaminations and degradations of the polymer in the flow channel. In this chapter, an enhanced coextrusion system to reduce the material residence time is described.

4-2 Modeling

The schematic of the new coextrusion die is presented in Figure 4-1. It consists of feeding, diffusion, converging, and land zones. The diffusion zone, where molecular diffusion of small molecular weight additives take place, is characterized by an expanded radial dimension, whereas it was only a long tube attached at the bottom of a coextrusion die in the previous case. As in the previous die and tube design, core and cladding materials are fed into the die by separate feeders. As before, the interface position can be adjusted by controlling relative flow rates from each feeder.

Diffusional flux of the additives across the core-cladding interface is significantly enhanced by the radially expanded geometry of the diffusion zone. As will be discussed

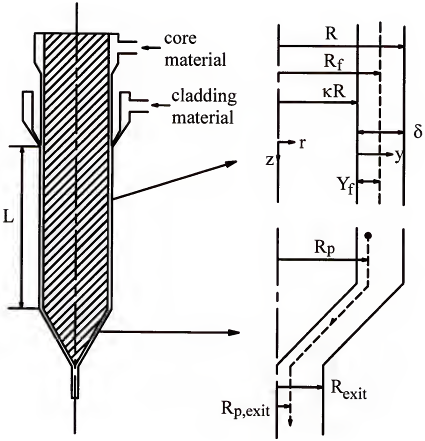

Figure 4-1. Schematic diagram of an annulus coextrusion die.

shortly, the increase in the contact area between core and cladding materials contributes to the higher diffusional flux of the additives across the interface.

When the gap in which the fluids are flowing is much small compared to the outer radius of the annulus (i.e., $\delta \ll R$ or κR), this system can be approximated by the flow between two parallel flat plates separated by distance δ, and equation 2-1 gives the following dimensionless equation in a Cartesian coordinate system:

$$6y(1-y)\frac{\partial x}{\partial z} = k^2 \frac{\partial^2 x}{\partial y^2} \qquad (4\text{-}1)$$

Here the dimensionless parameters k^2 is defined as $1/\varepsilon^2 Pe$ and Pe is the Peclet number defined as UL/D_A as in the tubular flow case and the small parameter ε is δ/R. R and L are the outer radius and the length of the diffusion zone. The scalings for the nondimensionalization are the same as those in Chapter 2 except that the transverse coordinate y is scaled by δ. It is also assumed that the rheological properties of the fluids are not altered by additives and the fluids are Newtonian. This assumption can be justified since it has little effect on the additive concentration profiles as discussed later in this chapter. Under the given assumptions, the velocity field is parabolic, and the initial and boundary conditions are

$$\begin{aligned} x(y,0) &= 1 \quad \text{when } y \le Y_\mathrm{f} \\ x(y,0) &= 0 \quad \text{when } y > Y_\mathrm{f} \end{aligned} \tag{4-2}$$

$$\left.\frac{\partial x}{\partial y}\right|_{y=1} = 0 \tag{4-3}$$

$$\left.\frac{\partial x}{\partial y}\right|_{y=0} = 0 \tag{4-4}$$

Equation 4-2 indicates the step concentration profile at the inlet to the diffusion zone (i.e., at $z = 0$). Here Y_f is the location of the interface between the core and the cladding, and equations 4-3 and 4-4 are the no flux conditions at both walls. Following the similar procedure as the problem in Chapter 2, the concentration profile was derived as

$$x = Y_\mathrm{f}^{\,2}\left(3 - 2Y_\mathrm{f}\right) + \sum_{n=1}^{\infty} \frac{2}{\beta_n} \frac{\left(\dfrac{dF_n}{dy}\right)_{y=Y_f}}{\left[F_n \dfrac{\partial}{\partial y}\left(\dfrac{\partial F}{\partial \beta}\right)_n\right]_{y=1}} e^{-\frac{\beta_n^{\,2}}{6}k^2 z} F_n(y,\beta) \tag{4-5}$$

The detailed derivation of the equation 4-5 is presented in Appendix B.

In order to convert concentration profiles at the end of the diffusion zone obtained by equation 4-5 to those at the die exit, the coordinate transformation was carried out as described below.

The velocity profile of a Newtonian fluid in an annulus is given by[57]

$$u = \frac{\Delta p R^2}{4\mu L}\left[1 - \left(\frac{r}{R}\right)^2 + \left(\frac{1-\kappa^2}{\ln(1/\kappa)}\right)\ln\left(\frac{r}{R}\right)\right] \tag{4-6}$$

and the flow rate is

$$Q = \frac{\pi \Delta p R^4}{8\mu L}\left[\left(1-\kappa^4\right) - \frac{\left(1-\kappa^2\right)^2}{\ln(1/\kappa)}\right] \tag{4-7}$$

If we follow a fluid particle p moving from the diffusion zone to the land zone, the flow rate in the inner annulus enclosed by the inner wall and the cylinder with radius R_p in the diffusion zone should be the same as the flow rate in the inner tube with the radius $R_{p,exit}$ since there is no bulk motion in the radial direction both in the diffusion and land zones (Figure 4-1):

$$\begin{aligned} &2\pi \int_{\kappa R}^{R_p} \frac{2Q}{\pi R^2}\left[(1-\kappa^4) - \frac{\left(1-\kappa^2\right)^2}{\ln(1/\kappa)}\right]^{-1}\left[1 - \left(\frac{r}{R}\right)^2 + \left(\frac{1-\kappa^2}{\ln(1/\kappa)}\right)\ln\left(\frac{r}{R}\right)\right] r\,dr \\ &= 2\pi \int_0^{R_{p,exit}} \frac{2Q}{\pi R_e^{\,2}}\left[1 - \left(\frac{r}{R_e}\right)^2\right] r\,dr \end{aligned} \tag{4-8}$$

New radial coordinates at the die exit corresponding to the radial coordinates at the annulus were calculated by integrating equation 4-8 and numerically solving the resulting algebraic equation.

The additive concentration profile described by equation 4-5 and 2-7 are compared in Figure 4-2 for several different cases. The solid line is the concentration profile of the

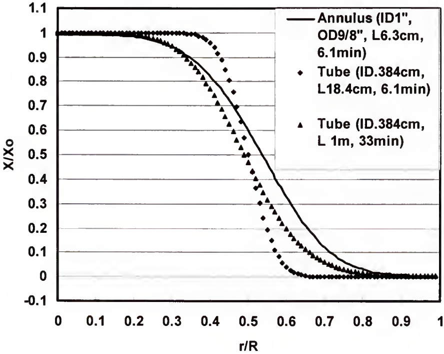

Figure 4-2. Additive concentration profiles
D_A 1.0×10^{-6} cm^2/s, Q 100g/hr
Line: Annulus, ID 1″, OD 1.125″, length 6.35 cm, residence time 6.1 min, k^2 0.008
◆ Tubular flow, ID 0.384 cm, length 18.4 cm, residence time 6.1 min, k^2 0.024
▲ Tubular flow, ID 0.384 cm, length 1 m, residence time 33 min, k^2 0.043

fiber obtained from the annular die with the inner diameter 1″ and the annulus gap width 1/16″, and the other two are for those obtained by the tubular extension described in Chapters 2 and 3. The diffusivity of the additive is 10^{-6} cm^2/sec, and the initial interface positions Y_f (or R_f for tubular flow) are 0.5. The flow rates are the same for all three cases as 100 g/hr, and the residence times were varied by changing the length of the diffusion zone.

Additive concentrations obtained with the annular design shows much broader profile despite the short residence tome of only 6 minutes in the diffusion zone, compared to the profile from the tubular design with the same residence time. The results indicate that the residence time required for the tubular design to obtain the profile close to that from annular design at the same temperature should be about 6 times larger. This means that the length of the diffusion zone should be 18 times longer because the average z-directional velocities of fluid elements in the diffusion zones are 1 cm/min and 3 cm/min for annulus and tube, respectively in these geometries.

Since the additive flow in the radial direction at the interface is the flux multiplied by the surface area across which additive molecules diffuse, the flow of the additive is greatly enhanced by expanding the tube to an annulus.

Due to the combined effects of the lowered velocity and the enhanced radial diffusion of the additive, the annulus design provides very effective means of producing GRIN profiles.

4-3 Reliability of the Approximate Solutions

Since the solution given in equation 4-5 is an approximate solution to the real annulus geometry, there is a finite amount of error involved, and the error in the approximate solution is expected to be order ε from the following asymptotic analysis. Starting from equation 2-1, the dimensionless governing equation in cylindrical coordinate system is expressed as

$$\begin{aligned}&\frac{3}{\varepsilon^2}\left[1-(1-\varepsilon+\varepsilon y)^2+\left(\frac{1-(1-\varepsilon)^2}{\ln(1/(1-\varepsilon))}\right)\ln(1-\varepsilon+\varepsilon y)\right]\frac{\partial x_{\mathrm{A}}}{\partial z}\\&=k^2\left(\frac{\partial^2 x_{\mathrm{A}}}{\partial y^2}+\frac{\varepsilon}{1-\varepsilon+\varepsilon y}\frac{\partial x_{\mathrm{A}}}{\partial y}+\varepsilon^2\frac{\partial^2 x_{\mathrm{A}}}{\partial z^2}\right)\end{aligned} \qquad (4\text{-}9)$$

By expanding the solution to an asymptotic series with the small parameter ε as in equation 4-10 and plug it into equation 4-9, we obtain the same equation as equation 4–1 for the leading order equation, and 4-11 for the order ε equation.

$$x_{\mathrm{A}} = x_{\mathrm{A}}^{(0)} + \varepsilon x_{\mathrm{A}}^{(1)} + \varepsilon^2 x_{\mathrm{A}}^{(2)} + \cdots \tag{4-10}$$

$$6y(1-y)\frac{\partial x_{\mathrm{A}}^{(1)}}{\partial z} + y(1-3y+2y^2)\frac{\partial x_{\mathrm{A}}^{(0)}}{\partial z} = k^2\left(\frac{\partial^2 x_{\mathrm{A}}^{(1)}}{\partial y^2} + \frac{\partial x_{\mathrm{A}}^{(0)}}{\partial y}\right) \tag{4-11}$$

In equation 4-10, subscripts (0), (1), and (2) denote the leading order, first order, and second order solutions. It can be noted that the order ε equation has the same form as the

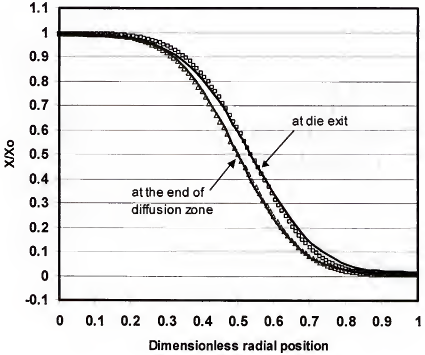

Figure 4-3. Comparison of analytic and numerical solutions
D_{A} 1.0×10^{-6} cm^2/s
Annulus ID 1″, OD 1.125″, length 6.35 cm, residence time 6.1 min
Lines: numerical solutions, Squares and triangles: analytic

leading order equation except the fact that it is inhomogeneous. Instead of solving the order ε equation to estimate the error in the leading order solution, numerical solutions for the original annulus geometry were obtained by the finite element analysis using Polyflow by Fluent Inc.

In Figure 4-3, the numerical solution is compared to the analytic solution of the asymptotic analysis. They show very close match, although the numerical solution of the entire flow domain including the converging and land zones (where additive diffusion also takes place) shows a slightly broader profile. This is because the analytic solution does not account for the diffusion taking place in the converging and land zones. Considering that the small parameter is as big as 1/8, this close match of the approximate solutions with the numerical solutions is noteworthy supporting the convenience of using the approximate analytic solutions.

4-4 Non-Newtonian Effect

Although we assumed a Newtonian fluid for the analysis, polymeric melts are not Newtonian.[58, 59] In Figure 4-4, concentration profiles obtained numerically assuming Newtonian and power-law fluids are compared. The power law model, given by equation 4-12 is not only easy to apply, but also describes the fluid properties reasonably well, especially in a small shear rate range.

$$\eta = m\dot{\gamma}^{n-1} \tag{4-12}$$

In the shear rate range of our interest (0.1 – 10 sec^{-1}), the power law index n of PMMA was found to be 0.8,[38] which means the shear rate dependence of viscosity is very weak. Consequently, concentration profile of power-law fluid is little different from that of Newtonian as shown in Figure 4-4. Therefore, Newtonian assumptions used in the present analysis for the diffusion-assisted coextrusion process is plausible.

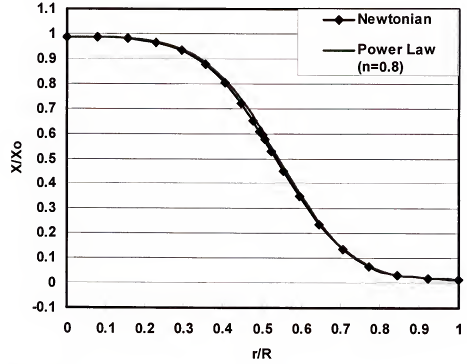

Figure 4-4. Concentration profiles of additives for Newtonian and power-law fluids in the annulus diffusion-assisted coextrusion process, D_A 1.17×10^{-6} cm^2/s, ID 1″, OD 1.125″, length 6.35 cm, Y_f 0.5

4-5 Experimental

The master batch chips containing 20 wt % DPS and DPSO (Diphenyl sulfoxide) were prepared by the same procedures described in Chapter 3. Diphenyl sulfoxide, whose molecular structure is shown in Figure 4-5, has a slightly larger molecular weight (202) and lower refractive index (1.606) than DPS. Therefore, It is expected to have lower diffusivity than DPS in the same polymer matrix at the same temperature. It is also

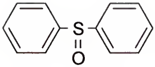

Figure 4-5 Molecular structure of DPSO

reported that PMMA-base GRIN POFs doped with DPSO maintain refractive index profiles after 12000 hours of heat treatment at 85 °C as the DPS-doped GRIN POFs.[37]

The annulus coextrusion die was designed based on the previous calculations in such a way that produces additive concentrations close to a parabolic profile in the central

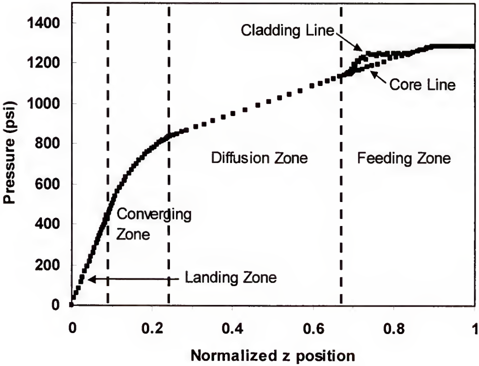

Figure 4-6. Pressure profile of PMMA melt at 200 °C in the coextrusion die calculated by Polyflow for power-law fluid ($\eta_0 = 10^5$ Pa.s, $n = 0.8$). Annulus ID 1″, OD 1.125″, length 6.35 cm

region of the fiber, and that optimizes the pressure profile in the die as shown in Figure 4-6. The inner diameter of the annulus was 1″ with the gap of 1/16″ and the length of the diffusion zone was 2.5″. Most pressure drop occurs in the converging and land zone, and it decreases linearly at a much slower rate in the feeding and diffusion zone to ensure the flow uniformity around the annulus. This is the essential requirement in designing plastic extrusion dies.[60]

The flow rate range investigated was 93–245 g/hr, and the melt temperature range was 193–212 °C. Initial concentrations of DPS and DPSO in the core were 6.5 wt % and 7.5 wt %, respectively for the reasons described in Chapter 3. The concentration profiles were measured with FT-IR by the same procedures as in the case of tubular flow.

4-6 Results and Discussion

The concentration profiles of DPS in PMMA fibers obtained by annulus coextrusion are plotted in Figure 4-7 for various operating conditions. The flow rate 245 g/hr corresponds to 2.5 minutes of average residence time in the diffusion zone and 5.5 minutes for 110 g/hr. The diffusivity at each melt temperature was obtained by curve fitting of the measured data by the same procedures described in Chapter 3, and appeared consistent with the values calculated for the tubular diffusion. The profiles show that molecular diffusion of DPS took place in the PMMA matrix pretty much with this short-residence time design to give us near parabolic index profiles and high bandwidth GRIN fibers.

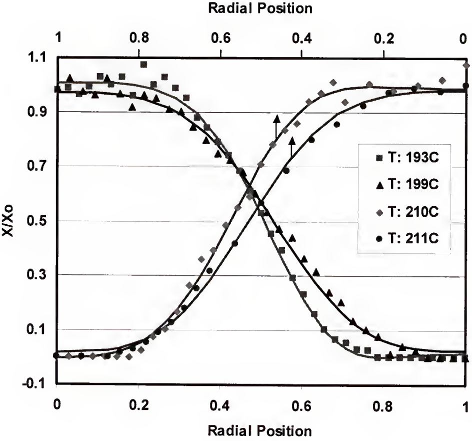

Figure 4-7 Concentration profiles for DPS-doped GRIN fiber obtained by annulus diffusion at different operating (lines: calculated, marlks: measured)
(a) ■ : melt T 193 °C, Q 153 g/hr, Y_f 0.47, D_A 1.17×10^{-6} cm^2/s, k^2 4.8×10^{-4}
(b) ▲ : melt T 199 °C, Q 110 g/hr, Y_f 0.495, D_A 1.66×10^{-6} cm^2/s, k^2 9.46×10^{-4}
(c) ◆ : melt T 209 °C, Q 245 g/hr, Y_f 0.54, D_A 2.25×10^{-6} cm^2/s, k^2 5.76×10^{-4}
(d) ● : melt T 211 °C, Q 175 g/hr, Y_f 0.555, D_A 2.42×10^{-6} cm^2/s, k^2 8.67×10^{-4}

The optimum profile that is closest to the parabolic profile in the fiber center can be obtained when k^2 value is about 8.5×10^{-4} (Figure 4-7d). When the k^2 value is smaller than this, the concentration profiles still have plateaus near the fiber axes, while the profile starts to flatten out at the center and outer edge of the fiber when k^2 value exceeds the optimum value, resulting in a lowered numerical aperture as shown in Figure 4-7(b).

In Figure 4-8, the concentration profiles of DPSO in PMMA obtained by annulus coextusion are plotted for various operating conditions. The flow rate and melt temperature ranges investigated were almost the same with the DPS case. However, the concentration profiles are stiffer than DPS doped fibers, implying that the diffusivity of DPSO is smaller than DPS as expected.

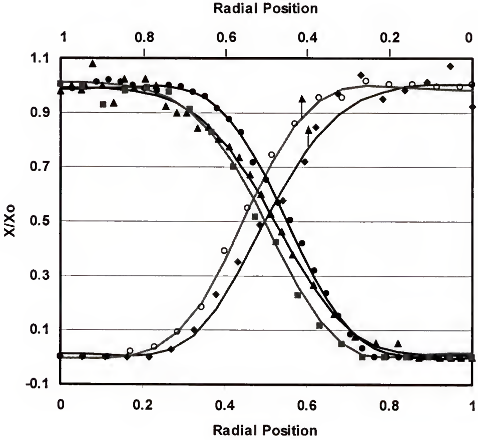

Figure 4-8 Concentration profiles for DPSO doped GRIN fiber obtained by annulus diffusion at different operating (lines: calculated, marlks: measured)

(a) ◆ : melt T 193 °C, Q 93 g/hr, Y_f 0.465, D_A 7.90×10^{-7} cm^2/s, k^2 5.33×10^{-4}
(b) ○ : melt T 198 °C, Q 128 g/hr, Y_f 0.52, D_A 9.10×10^{-7} cm^2/s, k^2 4.46×10^{-4}
(c) ● : melt T 201 °C, Q 176 g/hr, Y_f 0.53, D_A 1.28×10^{-6} cm^2/s, k^2 4.56×10^{-4}
(d) ▲ : melt T 210 °C, Q 151 g/hr, Y_f 0.488, D_A 1.65×10^{-6} cm^2/s, k^2 6.85×10^{-4}
(e) ■ : melt T 212 °C, Q 240 g/hr, Y_f 0.483, D_A 1.88×10^{-6} cm^2/s, k^2 4.91×10^{-4}

The diffusivities of DPS and DPSO in PMMA matrix at various temperatures calculated from the curve fittings of their concentration profiles using the model given by equation 4-5 were plotted in Figure 4-9. They show good linear dependencies on temperature in Arrhenius plots, and the diffusivities of DPSO are slightly lower than DPS as expected since it has larger molar volume than DPS. Their temperature dependences were estimated from the free volume theory as described in Chapter 3, and compared with the experimental values obtained from the linear regressions.

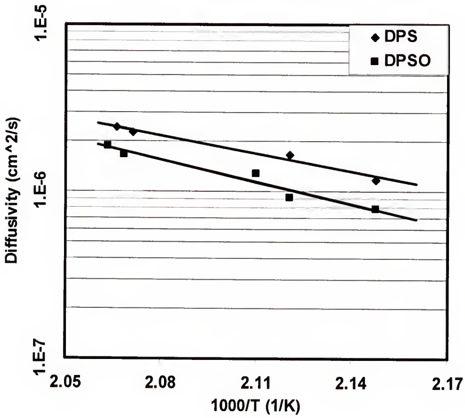

Figure 4-9 Diffusivities of DPS and DPSO in PMMA matrix at various temperatures (Points: from curve fitting of measured concentration, lines: linear regression lines).

The free volume parameters of PMMA and DPS used for the calculations are the same as listed in Table 3-1. For DPSO, van der Waals volume 139.39 cm^3/mole and the reciprocal of aspect ratio A/B 0.5858 calculated by the same procedures in Chapter 3 were used. The slopes of the regression lines are – 3.59, – 4.4, and calculated ones at 202°C were –3.5 and –4.4 for DPS and DPSO, respectively. They agree very well, and the slope of DPS is consistent with the results calculated in the previous chapter.

4-7 Estimation of Bandwidth

The bandwidths for the fibers prepared by annulus coextrusion with the refractive index profiles shown in Figure 4-7 and 4-8 were estimated by ray analysis. Following the same procedures described in Chapter 3, impulse response curves for 1 m long fibers were obtained and their bandwidths were calculated. The maximum refractive index was 1.500 for the DPS-doped fibers and 1.4985 for the DPSO-doped fibers at the fiber centers. The numerical apertures of these fibers were 0.164 and 0.160, respectively. The response curves presented in Figure 4-10 and 4-11 show that as the dimensionless parameter k^2 increases, and hence refractive index profile gets closer to parabolic, the response curve gets sharper and shifts to the left as pointed out in the previous chapters.

The bandwidths calculated either by 1/4σ and 0.45/FWHM from the response curves are listed in Table 4-1. Since the additive concentrations in the GRIN fibers are adjusted in such a way that the DPS-doped fiber and the DPSO-doped fiber have almost the same numerical apertures (0.164 and 0.160, respectively), the impulse response and bandwidth characteristics of the resulting fibers are determined only by the parameter k^2, and independent of the type of the dopants used.

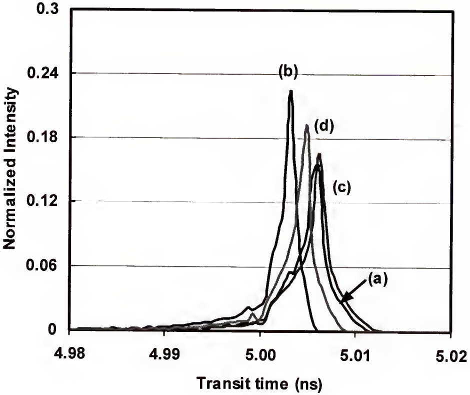

Figure 4-10 Impulse response curves for 1m long DPS-doped fibers (Numerical aperture: 0.164, refractive index at center: 1.5002). Curves (a), (b), (c), and (d) were calculated for the profile (a), (b), (c), and (d) in Figure 4-7, respectively.

As in the case of fibers fabricated by tubular flow design, the bandwidths calculated by the two methods show large differences in their magnitudes because the curve shapes are far from Gaussian. The maximum bandwidths over 700 MHz per 100 m by rms width method (or 2.5 GHZ by FWHM method) can be achieved when k^2 has the optimum value of 8.67×10^{-4} (Figure 4-7d and Figure 4-9d). Although the fiber with the refractive index profile in Figure 4-7b has a higher bandwidth than the one with the optimum profile, it is at the expense of numerical aperture, which is not desirable since one of the great advantages of POFs lies on their high numerical apertures.

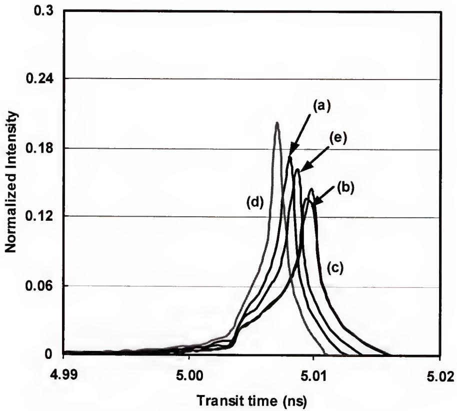

Figure 4-11 Impulse response curves for 1m long DPSO-doped fibers (Numerical aperture: 0.160, refractive index at center: 1.4996). Curves (a), (b), (c), (d), and (e) were calculated for the profile (a), (b), (c), (d), and (e) in Figure 4-8, respectively.

Table 4-1 Bandwidths obtained from rms width and FWHM for various refractive index profiles

Refractive Index Profile		Bandwidth (MHz per 100 m)	
		From rms width	From FWHM
NA 0.164 (Figure 4-10)	(a) k^2 4.80×10^{-4}	695	1930
	(b) k^2 9.46×10^{-4}	680	2845
	(c) k^2 5.76×10^{-4}	706	2189
	(d) k^2 8.67×10^{-4}	740	2500
NA 0.160 (Figure 4-11)	(a) k^2 5.33×10^{-4}	737	2290
	(b) k^2 4.46×10^{-4}	748	1873
	(c) k^2 4.56×10^{-4}	747	2055
	(d) k^2 6.85×10^{-4}	731	2880
	(e) k^2 4.91×10^{-4}	745	2233

4-8 Summary

The diffusion-assisted coextrusion process with an enhanced die design, where the radial dimension of the diffusion zone is expanded has been introduced to reduce the large residence time required for producing high bandwidth GRIN POFs by the tubular designs. A theoretical model for the process has been presented and verified experimentally by the fabrication of PMMA-base GRIN-POFs using DPS and DPSO as refractive index-modifying dopants, and measurements of the concentration profiles (refractive index profiles) by FT-IR spectroscopy.

It was found that the average residence time in the diffusion zone required to obtain desired index profiles are reduced by a factor of 1/6 compared to the tubular design by this approach, and the profiles can be controlled by the dimensionless parameter k^2. Due to the lowered velocity and the enhanced radial flow of the additive by increasing core-cladding interface area, the annulus design provides very effective means of producing GRIN profiles.

In addition, the diffusivities of dopants in PMMA matrix measured agree well with the measured values in tubular flow and the predictions from the free volume theory, and follow the Arrhenius law in the temperature range investigated.

The bandwidths of the GRIN POFs prepared thereby were estimated by ray analysis, and it was shown that bandwidth over 700 MHz per 100m with numerical aperture 0.164 could be obtained by this method.

CHAPTER 5
CONCLUSIONS

The diffusion-assisted coextrusion process has been introduced as a method to fabricate graded-index plastic optical fibers. In this process, two or more polymeric materials containing refractive-index-modifying additives are fed separately into a coextrusion die where a concentric multi-layer structure is formed. The multi-layered materials then proceed into a diffusion zone, where the additives diffuse forming a desired concentration (or refractive index) profile.

Theoretical analysis for the refractive index profile indicates that a large residence time in the diffusion zone is required to obtain a near-parabolic refractive index profile by this method. However, the refractive index profile can be altered significantly by adopting multi-layer approach and the annulus design of the diffusion zone. Furthermore, the bandwidth estimated by the ray analysis indicates that even a small variation of the refractive index profile created by the additive diffusion can result in a significant increase in the bandwidth compared to that of the SI-POF with sharp interfaces.

The concentration profiles were found to be strongly affected by the diffusivities of dopants, and can be controlled by varying the dimensionless parameter k^2, which contains the flow geometry, material properties and processing variables all together.

In addition, the diffusivities of the dopants in PMMA matrix showed Arrhenius type temperature dependence in the temperature range with the good agreements with the estimated values from the free volume theory, and the diffusivities were found to be 10^{-7}–10^{-6} cm^2/s range, which is consistent with the predictions of the theory.

By the annulus design, where the diffusion zone is a radially expanded annulus form, the large residence time requirements in the tubular designs could be relaxed. Due to the lower velocity and the enhanced radial diffusion of the additive by increasing core-cladding interface area, the annulus design provides very effective means of producing GRIN profiles. It was found that the average residence time in the diffusion zone required to obtain desired index profiles are considerably reduced compared to the tubular design by this approach, which is advantageous not only for the productivity, but also for the prevention of contamination and degradation of the material. The index profiles could be controlled by the dimensionless parameter k^2, and the optimum value were found to be 8.5×10^{-4} for the prescribed geometry.

The bandwidths of the GRIN POFs prepared thereby with a numerical aperture of 0.164 and 0.160 were estimated by ray analysis, and it was found that the impulse response curves for the GRIN POFs fabricated by the diffusion-assisted coextrusion process show significantly different shapes from Gaussian with very sharp peaks and long tails. Consequently, bandwidths estimated by FWHM were much higher than those from widely used rms widths of the response curves by the factor of three or more. Considering that the FWHM bandwidths have more significant implications in the real data communications, GRIN POFs fabricated by this method have good potential for communication applications.

Finally, it was shown through the theoretical analysis and experimental verifications that bandwidth over 700 MHz per 100 m could be obtained by this method, suggesting that the diffusion-assisted coextrusion process is a viable method to fabricate GRIN POFs with high bandwidths for the applications of short-distance communications.

APPENDIX A
DERIVATION OF SERIES SOLUTION IN CYLINDRICAL COORDINATE SYSTEM

Using the method of separation of variables [i.e., $x(z,r)=Z(z)F(r)$], eq 2-3 can be reduced to the following set of ordinary differential equations:

$$\frac{2}{k^2}\frac{1}{Z}\frac{dZ}{dz}=\frac{1}{(1-r^2)F}\left(\frac{d^2F}{dr^2}+\frac{1}{r}\frac{dF}{dr}\right)=-\beta^2 \tag{A-1}$$

The solution to the first equation for Z is given as

$$Z=Ne^{-\frac{\beta^2k^2}{2}z} \tag{A-2}$$

Following the approach described in Graetz, the second equation is transformed into the following form by setting $w = r\beta$:

$$\frac{d^2F}{dw^2}+\frac{1}{w}\frac{dF}{dw}+\left(1-\frac{w^2}{\beta^2}\right)F=0 \tag{A-3}$$

A series solution of the following form is then sought

$$F(w)=\sum_{i=0}^{\infty}B_{2i}w^{2i} \tag{A-4}$$

Substitution of eq A-4 into eq A-3 gives following recurrence formula for the coefficients B_{2i} of the series solution:

$$B_0=1,\quad B_2=-\frac{1}{4},\quad B_{2i}=\frac{1}{(2i)^2}\left(\frac{1}{\beta^2}B_{2i-4}-B_{2i-2}\right)\quad (i=2,3,\ldots) \tag{A-5}$$

This recurrence formula gives

$$B_{2i} = \sum_{j=0}^{\mathrm{int}\left(\frac{i}{2}\right)} a_{ji}\beta^{-2j}r^{2i} \tag{A-6}$$

Thus,

$$F = \sum_{i=0}^{\infty} \sum_{j=0}^{\mathrm{int}\left(\frac{i}{2}\right)} a_{ji}\beta^{2i-2j}r^{2i} \tag{A-7}$$

where

$$\begin{aligned} a_{00} &= 1 \\ a_{01} &= -1/4 \\ a_{0j} &= \frac{1}{(2j)^2}a_{0(j-1)} \quad \text{for } j \geq 2 \\ a_{ij} &= \frac{1}{(2j)^2}(a_{(i-1)(j-2)} - a_{i(j-1)}) \text{ for } i \geq 1 \text{ and } j \geq 2i \end{aligned} \tag{A-8}$$

int(i/2) in the upper bound of the summation sign in eq A-7 represents the integral part of the value i/2.

The boundary condition 2-6 indicates that β's are solutions to $F'(\beta) = 0$. Substitution of eq A-7 into eq 2-6 with eq A-8 gives the eigenvalues β_n as 5.0675, 9.1576, 13.1972, 17.2202, 21.2355, etc., and the eigenfunctions F_1 to F_5 corresponding to the eigenvalues β_1 to β_5 are shown in figure A-1.

When eqs A-2 and A-7 are combined, the solution is given as

$$x = \sum_{n=1}^{\infty} N_n e^{-\frac{\beta_n^2}{2}k^2 z} F_n(r,\beta) + C_0 \tag{A-9}$$

One remaining task to complete the solution is the determination of N_n. Since the governing equation is a Sturm-Louville type with the weighting function $r(1-r^2)$, the eigenfunctions are orthogonal, satisfying the following relations:

$$\int F_n F_m r\left(1-r^2\right)dr = 0 \quad if \quad n \neq m \tag{A-10}$$

and

$$\int_0^1 F_n F_n r(1-r^2)dr = \frac{1}{2\beta_n}\left[\left(\frac{\partial F}{\partial \beta}\right)_n \frac{\partial F}{\partial r} - F_n \frac{\partial}{\partial r}\left(\frac{\partial F}{\partial \beta}\right)_n\right]_{r=1} \tag{A-11}$$

Thus, the coefficients N_n is determined by multiplying each side of eq A-9 by $F_m r(1-r^2)$, and integrating from 0 to 1, and applying the initial condition 2-5:

$$\int_0^{R_f} F_n r(1-r^2)dr = N_n \int_0^1 F_n^{\,2} r(1-r^2)dr + C_0 \int_0^1 F_n r(1-r^2)dr \tag{A-12}$$

From eq A-3,

$$F_n r(1-r^2)dr = -\frac{1}{\beta_n^{\,2}} d\left(r\frac{dF_n}{dr}\right) \tag{A-13}$$

Therefore, from eqs A-10 through A-13, the coefficient N_n can be derived as

$$N_n = \frac{2}{\beta_n}\frac{R_f\left(\frac{dF_n}{dr}\right)_{r=R_f}}{\left[F_n \frac{\partial}{\partial r}\left(\frac{\partial F}{\partial \beta}\right)_n\right]_{r=1}} \tag{A-14}$$

Finally, the constant C_0 is determined by applying the material balance of the additive. The total flux of the additive at the entrance of the diffusion zone should be the same as the total flux at infinite length where the concentration profile of the additive should be flattened out and equal to C_0. Hence, from eq A-9,

$$2\pi \int_0^{R_f} 2(1-r^2)rdr = 2\pi \int_0^1 2(1-r^2)C_0 rdr \tag{A-15}$$

which gives the final solution:

$$x = 2R_f^{\,2}\left(1-\frac{R_f^{\,2}}{2}\right) + \sum_{n=1}^{\infty} N_n e^{-\frac{\beta_n^{\,2}}{2}k^2 z} F_n(r,\beta) \tag{A-16}$$

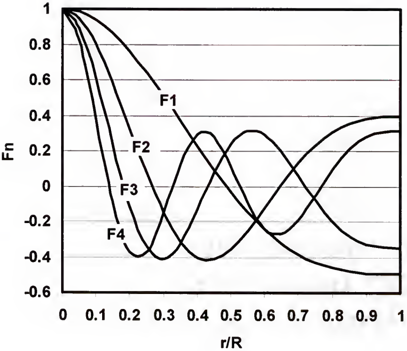

Figure A-1. Eigenfunctions F_1 through F_5 corresponding to eigenvalues β_1 through β_5.

APPENDIX B
DERIVATION OF SERIES SOLUTION IN CARTESIAN COORDINATE SYSTEM

Using the method of separation of variables [i.e., $x(z,y)=Z(z)F(y)$], eq 4-1 can be reduced to the following set of ordinary differential equations:

$$\frac{6}{k^2}\frac{1}{Z}\frac{dZ}{dz} = \frac{1}{y(1-y)F}\frac{d^2F}{dy^2} = -\beta^2 \tag{B-1}$$

The solution to the first equation for Z is given as

$$Z = Ne^{-\frac{\beta^2 k^2}{6}z} \tag{B-2}$$

Following the approach described in Appendix A, a series solution of the following form is then sought

$$F(y) = \sum_{i=0}^{\infty} B_i y^i \tag{B-3}$$

Substitution of eq B-3 into eq B-1 gives following recurrence formula for the coefficients B_i of the series solution:

$$\begin{aligned} &B_0 = 1,\ \ B_1 = 0,\ \ B_2 = 0,\ \ B_3 = -\frac{\beta^2}{6}, \\ &B_i = \frac{\beta^2}{i(i-1)}\left(B_{i-4} - B_{i-3}\right) \quad (i = 4,5,\ldots) \end{aligned} \tag{B-4}$$

This recurrence formula gives

$$B_i = \sum_{j=0}^{i} a_{ji}\beta^{2j} \tag{B-5}$$

Thus,

$$F = \sum_{i=0}^{\infty} \sum_{j=0}^{i} a_{ji} \beta^{2j} y^{i} \tag{B-6}$$

where

$$\begin{aligned} a_{00} &= 1 \\ a_{13} &= -1/6 \\ a_{ij} &= \frac{1}{j(j-1)} (a_{(i-1)(j-4)} - a_{(i-1)(j-3)}) \text{ for } i \geq 1 \text{ and } j \geq 4 \end{aligned} \tag{B-7}$$

Substitution of eq B-6 into eq 4-4 with eq B-7 gives the first three eigenvalues β_n as 9.05244, 17.1489, 25.1579. When eqs B-2 and B-6 are combined, the solution is given as

$$x = \sum_{n=1}^{\infty} N_n e^{-\frac{\beta_n^2}{6} k^2 z} F_n(y, \beta) + C_0 \tag{A-8}$$

Since the governing equation is a Sturm-Louville type with the weighting function $y(1-y)$, the eigenfunctions are orthogonal, satisfying the following relations:

$$\int F_n F_m y(1-y) dy = 0 \quad if \quad n \neq m \tag{B-9}$$

and

$$\int_0^1 F_n F_n y(1-y) dy = \frac{-1}{2\beta_n} \left[F_n \frac{\partial}{\partial y} \left(\frac{\partial F}{\partial \beta} \right)_n \right]_{y=0}^{y=1} \tag{B-10}$$

Thus, the coefficients N_n is determined by multiplying each side of eq B-8 by $F_m y(1-y)$, and integrating from 0 to 1, and applying the initial condition 4-2:

$$\int_0^{Y_f} F_n y(1-y) dy = N_n \int_0^1 F_n^2 y(1-y) dy + C_0 \int_0^1 F_n y(1-y) dy \tag{B-11}$$

From eq B-1,

$$F_n y(1-y) dy = -\frac{1}{\beta_n^2} d\left(\frac{dF_n}{dy} \right) \tag{B-12}$$

Therefore, from eqs B-9 through B-12, the coefficient N_n can be derived as

$$N_n = \frac{2}{\beta_n} \frac{\left(\frac{dF_n}{dy} \right)_{y=Y_f}}{\left[F_n \frac{\partial}{\partial y} \left(\frac{\partial F}{\partial \beta} \right)_n \right]_{r=1}} \tag{B-13}$$

Finally, the constant C_0 is determined by applying the material balance of the additive. The total flux of the additive at the entrance of the diffusion zone should be the same as the total flux at infinite length where the concentration profile of the additive should be flattened out and equal to C_0. Hence, from eq B-8,

$$\int_0^{Y_f} y(1-y)dy = \int_0^1 y(1-y)C_0 dy \tag{B-14}$$

which gives the final solution:

$$x = Y_f^{\,2}\left(3 - 2Y_f\right) + \sum_{n=1}^{\infty} N_n e^{-\frac{\beta_n^{\,2}}{6}k^2 z} F_n(y, \beta) \tag{B-15}$$

REFERENCES

(1) Senior, J. M. *Optical Fiber Communications*; Prentice Hall: London, U. K., 1985.

(2) Glen, R. M. Polymeric Optical Fiber. *Chemtronics* **1986**, *1*, 98.

(3) Theis, J.; Brockmeyer, A.; Groh, W.; Stehlin, T. F. *Polymer Optical Fibers in Data Communications and Sensor Applications*; Marcel Dekker: New York, 1992.

(4) Kaino, T. *Polymer Optical Fibers*; Marcel Dekker: New York, 1992.

(5) Snyder, A. W.; Love, J. D. *Optical Wave Guide Theory*; Chapman and Hall: London, U. K., 1983.

(6) Born, M.; Wolf, E. *Principles of Optics*, 6th ed.; Pergamon Press: New York, 1999.

(7) Koike, Y. High-Bandwidth Graded-Index Polymer optical Fiber. *Polymer* **1991**, *32*, 1737.

(8) Halley, P. *Fiber Optic Systems*; John Wiley & Sons: Chichester, U.K., 1987.

(9) Pollock, C. R. *Fundamentals of Optoelectronics*; Irwin: Chicago, IL, 1995.

(10) Ishigure, T.; Nihei, E.; Koike, Y. Optimum Refractive-Index Profile of the Graded-Index polymer Optical Fiber, toward Gigabit Data Links. *Applied Optics* **1996**, *35*, 2048.

(11) Ishigure, T.; Nihei, E.; Koike, y. Optimization of the Refractive-Index Distribution of High-Bandwidth GI Polymer Optical Fiber Based on Both Modal and Material Dispersions. *Polymer Journal* **1996**, *28*, 272.

(12) Ishigure, T.; Koike, Y.; Fleming, J. W. Optimum Index Profile of the Perfluorinated Polymer-Based GI Polymer Optical Fiber and Its Dispersion Properties. *Journal of Lightwave Technology* **2000**, *18*, 178.

(13) Kaino, T.; Jinguji, K.; Nara, S. Low Loss Poly(Methyl Methacrylate-d8) Core Optical Fibers. *Applied Physics Letters* **1983**, *42*, 567.

(14) Hornak, L. A. *Polymers for Lightwave and Integrated Optics*; Marcel Dekker: New York, 1992.

(15) Koike, Y.; Ishigure, T.; Nihei, E. High-Bandwidth Graded-Index Polymer Optical Fiber. *Journal of lightwave Technology* **1995**, *13*, 1475.

(16) Koike, Y.; Hatanaka, H.; Ohtsuka, Y. Studies on the Light-Focusing Plastic Rod. 17: Plastic GRIN Rod Lens Prepared by Photocopolymerization of a Ternary Monomer System. *Applied Optics* **1984**, *23*, 1779.

(17) Ishigure, T.; Nihei, E.; Koike, Y. Graded-Index Polymer Optical Fiber for High-Speed Data Communication. *Applied Optics* **1994**, *33*, 4261.

(18) Ishigure, T.; Horibe, A.; Nihei, E.; Koike, Y. High-Bandwith, High-Numerical Aperture Graded-Index Polymer Optical Fiber. *Journal of Lightwave Technology* **1995**, *13*, 1686.

(19) Ishigure, T.; Nihei, E.; Yamazaki, S.; Kobayashi, K.; Koike, Y. 2.5 Gbit/s 100m Data Transmission Using Graded-Index Polymer Optical Fiber and High-Speed Laser Diode at 650nm Wavelength. *Electronics Letters* **1995**, *31*, 467.

(20) Ishigure, T.; Nihei, E.; Koike, Y.; Forbes, C. E. Large-Core, High-Bandwidth Polymer Optical Fiber for Near Infrared use. *IEEE Phtonics Technology Letters* **1995**, *7*, 403.

(21) Ishigure Takaaki; Sato, M.; Nihei, E.; Koike, Y. Graded-Index Polymer Optical Fiber with High Thermal Stability of Bandwith. *Japanese Journal of Applied Physics* **1998**, *37*, 3986.

(22) van Duijnhoven, F. G. H.; Bastiaansen, C. W. M. Monomers and Polymers in a Centrifugal Field: A New Method to Produce Refractive-Index Gradients in Polymers. *Applied optics* **1999**, *38*, 1008.

(23) Park, C. W.; Lee, B. S.; Walker, J. K.; Choi, W. Y. A New Processing Method for the Fabrication of Cylindrical Objects with Radially Varying Properties. *Ind. Eng. Chem. Res.* **2000**, *39*, 79.

(24) Ho, B. C.; Chen, J. H.; Chen, W.-C.; Chang, Y.-H.; Yang, S. Y.; Chen, J. J.; Tseng, W. T. W. Gradient-Index Polymer Fibers Prepared by Extrusion. *Polymer Journal* **1995**, *27*, 310.

(25) Chen, W. C.; Chen, J. H.; Yang, S. Y.; Cherng, J. Y.; Chang, Y. H.; Ho, B. C. Preparation of Gradient-Index (GRIN) Polymer Fibers for Imaging Application. *Journal of Applied Polymer Science* **1996**, *60*, 1379.

(26) Chen, W.-C.; Chang, Y.; Hsu, J.-P. Theoretical Analysis on a Multilayer Coextrusion Process for Preparing Gradient-Index Polymer Optical Fibers. *Journal of Physical Chemistry B* **1999**, *103*, 7584.

(27) Liu, B.-T.; Chen, W.-C.; Hsu, J.-P. Mathematical Modeling of a Co-extrusion Process for Preparing Gradient-Index Polymer Optical Fibers. *Polymer* **1999**, *40*, 1451.

(28) Liu, B.-T.; Hsieh, M.-Y.; Chen, W.-C.; Hsu, J.-P. Gradient-Index Polymer Optical Fiber Preparation Through a Co-extrusion Process. *Polymer Journal* **1999**, *31*, 233.

(29) Jakob, M. *Heat Transfer*, 8th ed.; John Wiley & Sons: New York, 1962.

(30) Siegel, R.; Sparrow, E. M.; Hallman, T. M. Steady Laminar Heat Transfer in a Circular Tube with Prescribed Wall Heat Flux. *Applied Scientific Research* **1958**, *A7*, 386.

(31) Olshansky, R.; Keck, D. B. Pulse Broadening in Graded-Index Optical Fibers. *Applied Optics* **1976**, *15*, 483.

(32) Barrell, K. F.; Pask, C. Impulse Response Calculation: Invitation to a Problem in Numerical Integration. *Interational Journal of Computer Mathematics* **1980**, *8* , 167.

(33) Garito, A. F.; Wang, J.; Gao, R. Effects of Random Perturbations in Plastic Optical Fibers. *Science* **1998**, *281*, 962.

(34) Ishigure, T.; Kano, M.; Koike, Y. Propagating Mode Attenuation and Coupling Characteristics of Graded-Index POF. *Proceedings of the 8th International POF Conference*, Chiba, Japan,

(35) Yabre, G. Theoretical Investigation on the Dispersion of Graded-Index Polymer Optical Fibers. *Journal of Lightwave Technology* **2000**, *18*, 869.

(36) Ankiewicz, A. Comparison of Wave and Ray Techniques for Solution of Graded Index Optical Waveguide Problems. *Optica Acta* **1978**, *25*, 361.

(37) Sato, M.; Ishigure, T.; Koike, Y. Thermally Stable High-Bandwidth Graded-Index Polymer Optical Fiber. *Journal of Lightwave Technology* **2000**, *18*, 952.

(38) Rohm & Haas Technical Data on PMMA molding Compound, Darmstadt, Germany, 1997.

(39) Ingle, J. D.; Crouch, S. R. *Spectrochemical Analysis*; Prentice Hall: New York, 1998.

(40) Mauritz, K. A.; Storey, R. F.; George, S. E. A General Free Volume Based Theory for the Diffusion of Large Molecules in Amorphous Polymers above Tg. 1. Application to Di-n-alkyl Phthalates in PVC. *Macromolecules* **1990**, *23*, 441.

(41) Ehlich, D.; Sillescu, H. Tracer Diffusion at the Glass Transition. *Macromolecules* **1990**, *23*, 1600.

(42) Vrentas, J. S.; Vrentas C.M. A New Equation Relating Self-Diffusion and Mutual Diffusion Coefficients in Polymer-Solvent Systems. *Macromolecules* **1993**, *26*, 6129.

(43) Vrentas, J. S.; Vrentas C.M. Evaluation of Free-Volume Theories for Solvent Self-Diffusion in Polymer-Solvent Systems. *Journal of Polymer Science: Part B: Polymer Physics* **1993**, *31*, 69.

(44) Vrentas, J. S.; Vrentas C.M. Energy Effects for Solvent Self-Diffusion in Polymer-Solvent Systems. *Macromolecules* **1993**, *26*, 1277.

(45) Vrentas, J. S.; Vrentas C.M.; Duda, J. L. Comparison of Free-Volume Theories. *Polymer Journal* **1993**, *25*, 99.

(46) Vrentas, J. S.; Vrentas C.M. Solvent Self-Diffusion in Rubbery Polymer-Solvent Systems. *Macromolecules* **1994**, *27*, 4684.

(47) Vrentas, J. S.; Vrentas C.M.; Faridi, N. Effect of Solvent Size on Solvent Self-Diffusion in Polymer-Solvent Systems. *Macromolecules* **1996**, *29*, 3272.

(48) Vrentas, J. S.; Vrentas, C. M. Predictive Methods for Self-Diffusion and Mutual Diffusion Coefficients in Polymer-Solvent System. *European Polymer Journal* **1998**, *34*, 797.

(49) Bondi, A. *Physical Properties of Molecular Crystals, Liquids and Gasses*; John Wiley & Sons: New York, 1968.

(50) van Krevelin, D. W. *Properties of Polymers*, 3rd ed.; Elsevier : Amsterdam, The Netherlands, 1990.

(51) Porter, D. *Group Interaction Modeling of Polymer Properties*; Marcel Dekker: New York, 1995.

(52) Bicerano, J. *Prediction of Polymer Properties*; Marcel Dekker: New York, 1993.

(53) Rohrbaugh, R. H.; Jurs, P. C. Molecular Shape and the Prediction of High-Performance Liquid Chromatographic Retention Indexes of Polycyclic Aromatic Hydrocarbons. *Analytical Chemistry* **1987**, *59*, 1048.

(54) Berens, A. R.; Hopfenberg, H. B. Diffusion of Organic Vapors at Low Concentration in Glassy PVC, Polystyrene, and PMMA. *Journal of Membrane Science* **1982**, *10*, 283.

(55) Flipsen, T. A. C.; Pennings, A. J.; Hadziioannou, G. Polymer Optical Fiber with High Thermal Stability and Low Optical Losses Based on Novel Densely Crosslinked Polycarbosiloxanes. *Journal of Applied Polymer Science* **1998**, *67*, 2223.

(56) Arnaud, J. A. *Beam and Fiber Optics*; Academic Press: New York, 1976.

(57) Bird, R. B.; Steward, W. E.; Lightfoot, E. N. *Transport Phenomena*; John Wiley & Sons: New York, 1960.

(58) Bird, R. B.; Armstrong, R. C.; Hassager, O. *Dynamics of Polymeric Liquids: Volume 1 Fluid Mechanics*, 2nd ed.; John Wiley & Sons: New York, 1987.

(59) Ferry, J. D. *Viscoelastic Properties of Polymers*, 3rd ed.; John Wiley & Sons: New York, 1980.

(60) Michaeli, W. *Extrusion Dies for Plastics and Rubber*, 2nd ed.; Hanser Publishers: New York, 1991.

BIOGRAPHICAL SKETCH

In-Sung Sohn was born on September 22, 1965, in Seoul, Korea. He received his Bachelor of Science degree in chemical engineering from Seoul National University in 1988, and his Master of Science degree in chemical engineering from KAIST (Korea Advanced Institute of Science and Technology) in 1991. Then, he joined Saehan Ind., where he worked as a research engineer in the R&D center for 6 years. In 1994, he married Hyun-Su Lee, and had a daughter, Ye-Bin, in 1995. He started his study toward the Doctor of Philosophy degree at the University of Florida, Gainesville, in the fall of 1997.

I certify that I have read this study and that in my opinion it conforms to acceptable standards of scholarly presentation and is fully adequate, in scope and quality, as a dissertation for the degree of Doctor of Philosophy.

Chang Won Park

Chang-Won Park, Chair
Professor of Chemical Engineering

I certify that I have read this study and that in my opinion it conforms to acceptable standards of scholarly presentation and is fully adequate, in scope and quality, as a dissertation for the degree of Doctor of Philosophy.

Spyros A. Svoronos

Spyros Svoronos
Professor of Chemical Engineering

I certify that I have read this study and that in my opinion it conforms to acceptable standards of scholarly presentation and is fully adequate, in scope and quality, as a dissertation for the degree of Doctor of Philosophy.

Richard B. Dickinson
Associate Professor of Chemical Engineering

I certify that I have read this study and that in my opinion it conforms to acceptable standards of scholarly presentation and is fully adequate, in scope and quality, as a dissertation for the degree of Doctor of Philosophy.

Anthony B. Brennan

Anthony B. Brennan
Professor of Materials Science and Engineering

This dissertation was submitted to the Graduate Faculty of the College of Engineering and to the Graduate School and was accepted as partial fulfillment of the requirements for the degree of Doctor of Philosophy.

December 2001

Dean, College of Engineering

Dean, Graduate School